

## Table of contents

Résumé.....	iv
Acknowledgements .....	v
List of figures .....	viii
List of tables .....	x
Introduction .....	1
Chapter 1: Hydrogen Storage.....	2
1.1 Hydrogen as an energy carrier.....	2
1.1.1 Hydrogen storage systems .....	3
1.1.1.1 Compressed hydrogen gas .....	4
1.1.1.2 Liquid hydrogen .....	4
1.1.1.3 Systems based on physisorption of hydrogen .....	4
1.1.1.4 Metal hydride tanks.....	5
1.1.2 Metal Hydrides .....	5
1.1.3 Hydrogenation process .....	6
1.1.4 Thermodynamic properties of Metal Hydrides.....	8
1.1.5 Activation process.....	12
1.2 Ti-V-Cr BCC solid solution .....	13
1.3 Effect of a secondary phase.....	13
1.4 Objective of this research .....	14
Chapter 2: Experimental Methods .....	15
2.1. Arc Melting .....	15

2.2 Characterization of materials.....	16
2.2.1 Scanning Electron Microscopy (SEM) .....	16
2.2.2 Energy Dispersive X-ray spectroscopy (EDX).....	18
2.2.3 X-Ray Diffraction .....	19
2.2.4 Sievert's Apparatus.....	21
2.3 Synthesis and characterization of materials .....	22
Chapter 3: Microstructure and hydrogen storage properties of $\text{Ti}_{1.0}\text{V}_{0.9}\text{Cr}_{1.1}$ alloy with addition of x wt % Zr (x = 0, 2, 4, 8, and 12) .....	24
3.1 Introduction .....	24
3.2 Results and discussions .....	24
3.2.1 Microstructure Analysis.....	24
3.2.2 Structural Characterization .....	32
3.2.3 Activation process.....	34
3.2.4 XRD patterns after Hydrogenation .....	37
3.2.5 Air exposure effect.....	40
3.3 Conclusion.....	42
Chapter 4: The article.....	43
4.1 Abstract .....	43
4.2 The article.....	44
Conclusions and perspectives .....	56
REFERENCES.....	57

## List of figures

Figure 1.1: Hydrogen Fuel Cycle .....	2
Figure 1.2: Comparison of specific energies of different hydrocarbon fuels with that of hydrogen .....	3
Figure 1.3: Volume of 4 kg of hydrogen stored in different ways with size relative to car's size .....	5
Figure 1.4: Schematic Lennard-Jones potential energy diagram of hydrogen molecule and atom approaching hydride surface .....	7
Figure 1.5: Ideal Pressure-Composition-Isotherms (PCI) on the upper left-hand side, the construction of the corresponding Van't Hoff plot on the upper right-hand and on the lower part a schematic representation of hydrogen atoms (red) penetrating the metal host lattice (metals atoms are grey) in $\alpha$ , $\alpha+\beta$ and $\beta$ phases .....	9
Figure 1.6: Schematic presentation of sloping plateau, hysteresis and reversible capacity .....	12
Figure 2.1: Arc-melting furnace .....	16
Figure 2.2: Signals emitted from different parts of the interaction volume .....	17
Figure 2.3: Mechanisms of emission of secondary electrons, backscattered electrons, and characteristic X-rays from atoms of the sample .....	18
Figure 2.4: Diffraction of incident X-rays from the family of parallel atomic planes .....	19
Figure 2.5: Bruker D8 advance X-Ray diffractometer .....	20
Figure 2.6: Schematic of the hydrogen titration apparatus .....	21
Figure 3.1: Backscattered electrons (BSE) micrographs of: $\text{Ti}_1\text{V}_{0.9}\text{Cr}_{1.1} + x \text{ wt \% Zr}$ with $x = 0$ (a), 2 (b), 4 (c), 8 (d) and 12 (e) .....	25

Figure 3.2: Backscattered electrons micrographs of: $\text{Ti}_1\text{V}_{0.9}\text{Cr}_{1.1} + x$ wt % Zr alloys with elements mapping where $x=0$ (a), 2 (b), 4 (c), 8 (d) and 12 (e) .....	28
Figure 3.3: X-ray diffraction patterns of as cast: $\text{Ti}_1\text{V}_{0.9}\text{Cr}_{1.1} + x$ wt % Zr alloys with $x = 0, 2, 4, 8,$ and 12 .....	32
Figure 3.4: Activation curves of: $\text{Ti}_1\text{V}_{0.9}\text{Cr}_{1.1} + x$ wt % Zr for $x = 0, 2, 4, 8,$ and 12 at room temperature under 2 MPa of hydrogen .....	35
Figure 3.5: X-ray diffraction patterns of: $\text{Ti}_1\text{V}_{0.9}\text{Cr}_{1.1} + x$ wt % Zr alloys in the hydrogenated state for $x = 0, 2, 4, 8,$ and 12 .....	38
Figure 3.6: First hydrogenation curves of: $\text{Ti}_1\text{V}_{0.9}\text{Cr}_{1.1} + 12$ wt % Zr crushed under argon and under air and after 2 days of air exposure at room temperature and under 2 MPa of hydrogen .....	41

## List of tables

Table 3.1: Bulk atomic abundance: nominal and as measured by EDX of: $\text{Ti}_1\text{V}_{0.9}\text{Cr}_{1.1} + x$ wt % Zr alloys for $x = 0, 2, 4, 8$ and $12$ . Error on the last significant digit is indicated in parentheses .....	26
Table 3.2: EDX analysis showing the elemental composition of the matrix (point 1) of: $\text{Ti}_1\text{V}_{0.9}\text{Cr}_{1.1} + x$ wt % Zr alloys for $x = 0, 2, 4, 8$ and $12$ . Error on all values is $0.1$ at %.....	29
Table 3.3: EDX analysis showing the elemental composition of the secondary phase 1 (point 2) of $\text{Ti}_1\text{V}_{0.9}\text{Cr}_{1.1} + x$ wt % Zr alloys for $x = 0, 2, 4, 8$ , and $12$ .....	30
Table 3.4: EDX analysis showing the elemental composition of secondary phase 2 (point 3) of: $\text{Ti}_1\text{V}_{0.9}\text{Cr}_{1.1} + x$ wt % Zr alloys for $x = 0, 2, 4, 8$ , and $12$ .....	31
Table 3.5: EDX analysis showing the elemental composition at point 4 of: $\text{Ti}_1\text{V}_{0.9}\text{Cr}_{1.1} + x$ wt % Zr alloys for $x = 0, 2$ , and $4$ .....	31
Table 3.6: Crystal parameters and abundance of each phase in as cast: $\text{Ti}_1\text{V}_{0.9}\text{Cr}_{1.1} + x$ wt % Zr alloys for $x = 0, 2, 4, 8$ , and $12$ . Error on the last significant digit is indicated in parentheses .....	33
Table 3.7: Crystal parameters and abundance of each phase in hydrogenated: $\text{Ti}_1\text{V}_{0.9}\text{Cr}_{1.1} + x$ wt % Zr alloys for $x=0, 2, 4, 8$ and $12$ . Error on the last significant digit is indicated in parentheses .....	39

## Introduction

The use of hydrogen as a safe and efficient energy vector of the future requires overcoming barriers such as production cost and storage. The difficulties in hydrogen storage are still an important shortcoming for practical applications. Among the various storage means, metal hydrides are very interesting because of their high volumetric density, safety and reversibility. They can be operated at relatively low temperatures and pressures typical of fuel cell operation.

Amongst the different metal hydride systems, Ti-V-Cr body-centered-cubic (BCC) solid solution alloys are good candidates for hydrogen storage tanks because of their tunable plateau pressure, reasonable hydrogen storage capacity and safety. But, these alloys suffer from slow and difficult first hydrogenation, the so-called activation step. The first hydrogenation is usually done by subjecting the alloy to a high hydrogen pressure at high temperature which complexify and add cost to the hydride production.

The objective of this research was to study the effect of adding Zr to BCC alloy for quick activation. We used Zr as an additive because prior investigations showed that the alloy  $\text{Zr}_7\text{Ni}_{10}$  greatly enhance the first hydrogenation of Ti-V-Cr alloys. Using Zr instead of  $\text{Zr}_7\text{Ni}_{10}$  would mean a lower material cost and simpler system. We also investigated the effect of air exposure on the first hydrogenation.

This master's thesis is formed of four chapters. Chapter 1 is an introduction of the context of the study. Chapter 2 is a description of the experimental techniques used for the synthesis and characterization of materials. In chapter 3, the results of addition of Zr to  $\text{Ti}_1\text{V}_{0.9}\text{Cr}_{1.1}$  alloy are shown and discussed, and finally, chapter 4 displays our published article in the special issue of the journal *Inorganics*, entitled "Functional Materials Based on Metal Hydrides".

## Chapter 1: Hydrogen Storage

### 1.1 Hydrogen as an energy carrier

Our society is implementing more and more renewable energy sources such as wind energy, solar energy, etc. For solar and wind energies, the production is usually not in phase with the utilization, so a means to store and carry energy is needed. Hydrogen is a renewable energy carrier and could also be used as an energy storage [1, 2]. Its high gravimetric storage capacity attracted the attention of the researchers and increased their interest in hydrogen fuel and storage technologies.

Hydrogen doesn't exist freely in nature, it should be released from chemical compounds like hydrocarbons and water. There are many methods to produce hydrogen such as steam reforming of natural gas, gasification of coal and biomass, partial oxidation of hydrocarbons and electrolysis of water [3]. In the ideal hydrogen fuel cycle (from water to water) as presented in Figure 1.1, hydrogen is produced by splitting water via electrolysis using solar energy and is stored to produce electrical energy.

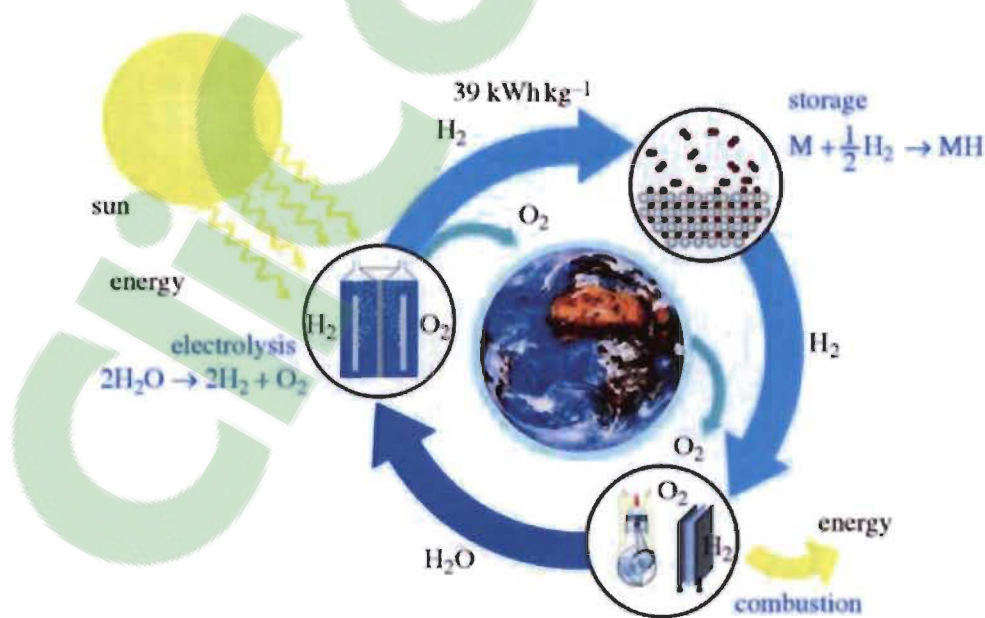
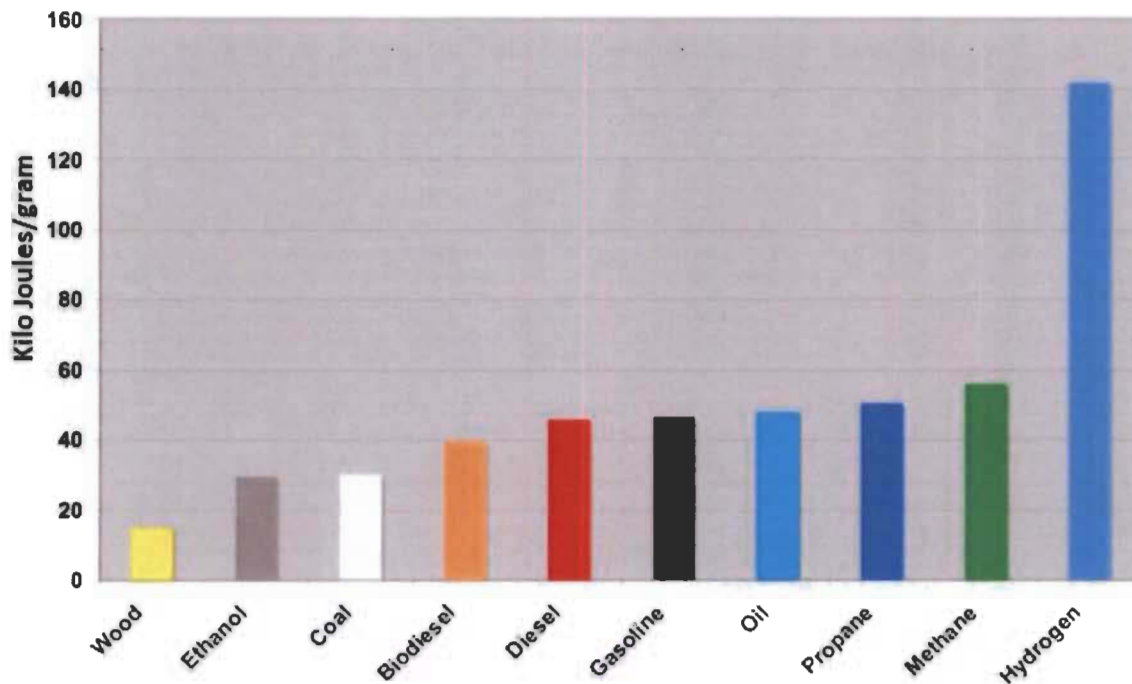


Figure 1.1: Hydrogen Fuel Cycle [4]

Since the by-product of hydrogen reaction in the fuel cell is water, it is environmentally friendly and can be adopted to secure a clean carbon-free energy for the future [5]. From the energy content point of view, the gravimetric energy density of hydrogen is 142 kJ/g which is about three times that of gasoline and almost five times higher than that of coal [6] as shown in Figure 1.2.



**Figure 1.2: Comparison of specific energies of different hydrocarbon fuels with that of hydrogen [7]**

However, the volumetric energy density of hydrogen at atmospheric pressure and room temperature is too low, 1 kg of hydrogen occupies a volume of 11 m<sup>3</sup>. Many efforts are being made in order to find new materials with high volumetric hydrogen storage capacity.

### **1.1.1 Hydrogen storage systems**

The hydrogen storage system for most practical applications should have a high storage capacity, high gravimetric and volumetric densities, long and stable cycling performance and safe operation.



Hydrogen can be stored using many ways such as: compressed hydrogen gas, liquid hydrogen, systems based on physisorption of hydrogen and metal hydride tanks.

#### **1.1.1.1 Compressed hydrogen gas**

Hydrogen is stored in its gaseous form at room temperature in cylinders that can withstand pressures up to 800 bars. At that pressure, the hydrogen volumetric density is  $40 \text{ kg/m}^3$  but the gravimetric density is low and this limits the practical use of compressed hydrogen cylinders. In addition, handling highly pressurised compressed cylinders implies safety risks [8].

#### **1.1.1.2 Liquid hydrogen**

Here, hydrogen is stored in its liquid form in cryogenic tanks at around  $-252^\circ\text{C}$  and at ambient pressure. Liquid hydrogen has a high volumetric density of  $70.8 \text{ g/L}$ . Despite the large amount of energy required for liquefaction, this method is being used to transport large quantities of hydrogen. However, hydrogen boil-off and the cost of advanced insulating tanks to maintain very low temperatures coupled with the energy cost to liquefy hydrogen make this method impractical for on-board vehicular application [9].

#### **1.1.1.3 Systems based on physisorption of hydrogen**

Molecular hydrogen can be adsorbed to the surface of porous materials by the weak Van der Waal forces. Thus, hydrogen molecules can be reversibly stored on high specific surface area materials such as carbon-based materials and Metal Organic-Frameworks (MOFs). The amount of hydrogen stored at  $77 \text{ K}$  and under 70 bars on porous carbon and MOFs materials have been found to be around 5 wt % and 7.5 wt % respectively. Usually, to get significant adsorption, a cryogenic temperature as well as high specific area and porosity are needed [10, 11].

#### 1.1.1.4 Metal hydride tanks

Atomic hydrogen can be stored in a metal hydride. In general, metal hydrides have higher hydrogen volumetric density at ambient conditions compared to the three storage systems mentioned previously. This is shown in Figure 1.3 which compares the volume needed to store hydrogen in: solid metal hydrides, liquified hydrogen and compressed hydrogen. It is shown that storing 4 kg of hydrogen requires an internal volume of 110 L in high-pressure tank, while liquified hydrogen requires about 57 L. In the case of metal hydrides, the volume needed is much less, being 33 L or 26 L depending on the type of hydride. From the practical point of view where reduction in volume is important, the storage of hydrogen in metal hydrides could be promising.

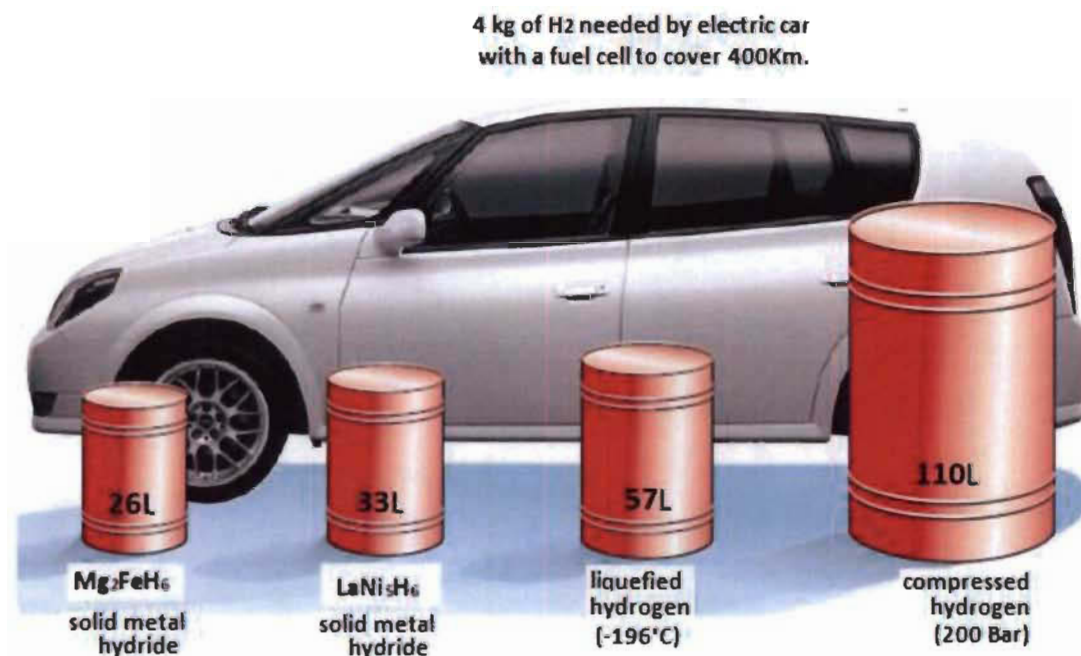


Figure 1.3: Volume of 4 kg of hydrogen stored in different ways with size relative to car's size [12]

#### 1.1.2 Metal Hydrides

The study of metal hydrides started with Thomas Graham nearly 150 years ago with the discovery of the hydrogen absorption properties of palladium [13].

Generally, hydride compounds can be formed with most transition elements and rare earths or actinides. In these compounds, hydrogen atom acts as a metal forming a chemical bond with the metal atoms in the bulk of material. Metal hydrides usually exhibit an important electrical resistivity compared to metals. They are commonly hard and brittle.

Intermetallic compounds have been extensively studied for hydrogen storage. These compounds are characterized by well-defined stoichiometric compositions and crystalline order. They are broadly classified as AB, AB<sub>2</sub> or AB<sub>5</sub> systems, where A is a stable hydride forming element like a transition metal from group III to VI or a rare earth element and B is a weak hydride forming element like Ni, Fe, Co, Al, etc [14]. According to Miedema's model of reversed stability, the more stable intermetallic compound of A and B, the less stable will be the corresponding hydride and vice versa [15].

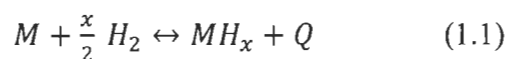
Intermetallic compounds, such as binary AB<sub>5</sub> alloys like LaNi<sub>5</sub>, have high volumetric hydrogen densities (115 kg/m<sup>3</sup>) and good cycling ability [16]. However, their gravimetric storage capacity is low (1.5 wt % H<sub>2</sub> in case of LaNi<sub>5</sub>H<sub>6</sub>) which is not suitable for on-board hydrogen storage. This is the main drawback for several other intermetallic hydrides having gravimetric capacities less than 4 wt % H<sub>2</sub>.

In the case of solid solution alloys, the metal atoms of the constituent elements are randomly arranged in the crystal lattice. TiVCr solid solutions with body centered cubic (BCC) structure are well known metal hydride alloys. They have been considered as candidate for hydrogen storage application due to their relatively high absorption capacity (3.0 wt %). More details on these alloys are given in Section 1.2.

As hydrides are formed by direct reaction with gaseous hydrogen, it is important to present the hydrogenation process and the thermodynamic properties of metal hydrides.

### 1.1.3 Hydrogenation process

Equation (1.1) represents metal hydride formation:



where  $M$  is a metal,  $MH_x$  is a hydride,  $x$  is the ratio of hydrogen atoms to metal atoms  $H/M$  and  $Q$  is the thermal energy released or heat of the reaction.

The hydrogenation mechanism can be divided into the following steps:

1. Adsorption of hydrogen molecules on the surface.
2. Dissociation to atomic hydrogen.
3. Diffusion of H atoms into the bulk of the metal (obeying Fick's law) forming a solid solution.
4. When hydrogen concentration exceeds a certain limit depending on the metal host, a hydride phase starts to nucleate.
5. Diffusion of hydrogen through the hydride layer.

Figure 1.4 represents the potential energy curves for dissociation and chemisorption of hydrogen on a clean metal surface.

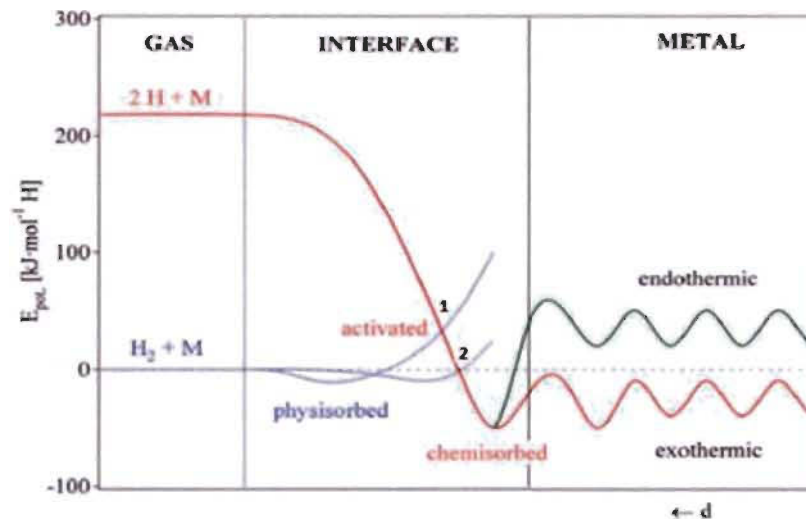


**Figure 1.4: Schematic Lennard-Jones potential energy diagram of hydrogen molecule and atom approaching hydride surface [17]**

When an hydrogen molecule is getting closer to the surface, the potential energy will increase due to repulsion between the electronic clouds of the molecule and the surface. Upon increasing the potential energy of the  $H_2$  molecule, it could intersect with the potential energy of the H atom (point 1 in Fig 1.4) and thus energetically favor for  $H_2$  molecule to dissociate into two H atoms and bonded to metal surface.

At point 1, the potential energy is positive, therefore dissociation occurs and the activation barrier is the height of point 1. The height of this barrier generally depends on the type of metal atoms at the surface.

If the intersection happens at point 2 where the potential energy is zero, then a fraction of  $H_2$  molecules of energy higher than the activation barrier will dissociate and the dissociation is said to be non-activated. After dissociation, the H atoms will be chemisorbed on the surface and bonded to the metal atoms.

This chemisorption is exothermic if the hydrogen-metal H-M bond is stronger than hydrogen-hydrogen H-H bond otherwise it will be endothermic.

#### **1.1.4 Thermodynamic properties of Metal Hydrides**

##### **The pressure composition isotherm (PCI)**

The thermodynamic aspects of the hydrogen absorption/desorption reaction are given by the temperature and pressure of the reaction.

Figure 1.5 (to the left) displays the PCI behavior of an ideal hydride.

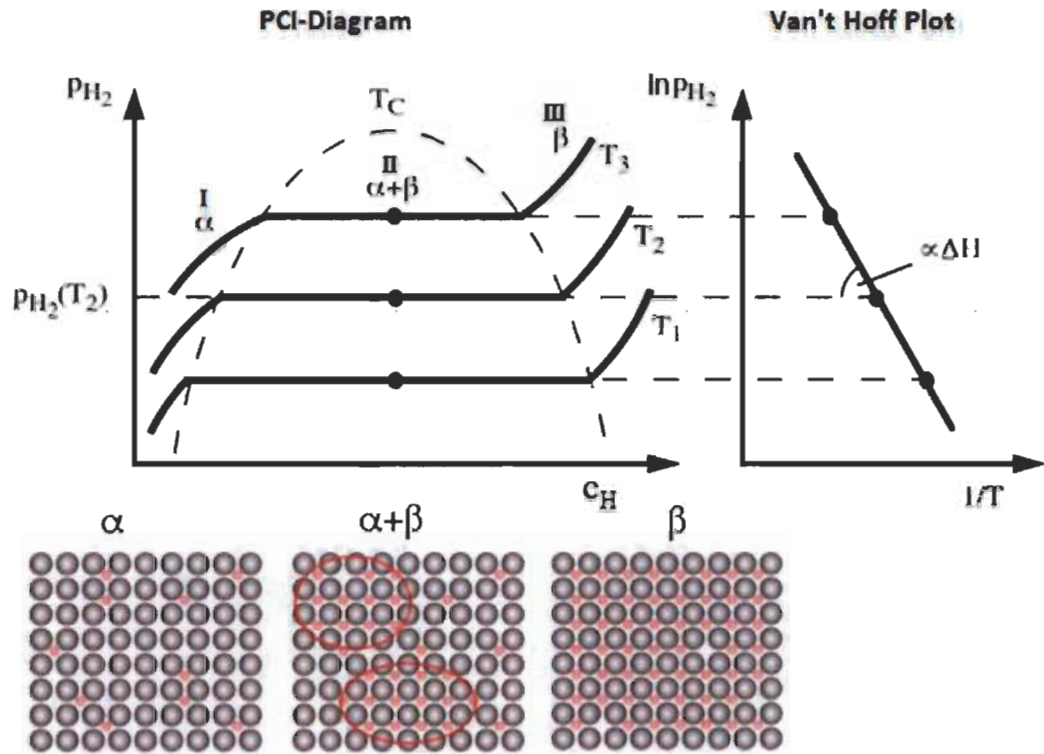


**Figure 1.5: Ideal Pressure-Composition-Isotherms (PCI) on the upper left-hand side, the construction of the corresponding Van't Hoff plot on the upper right-hand and on the lower part a schematic representation of hydrogen atoms (red) penetrating the metal host lattice (metals atoms are grey) in  $\alpha$ ,  $\alpha+\beta$  and  $\beta$  phases [14]**

Each isotherm, is a plot of equilibrium hydrogen pressure and hydrogen to metal ratio (concentration of hydrogen:  $C_H$ ) at a constant temperature, and could be divided into three regions I, II and III.

Referring to Gibb's phase rule, the degree of freedom  $F$  at constant temperature in each region is determined by the equation:

$$F = C - P + 2 \quad (1.2)$$

where  $C$  is the number of components of hydrogen-metal system and  $P$  is the number of phases in thermodynamic equilibrium with each other in this system.  $F$  provides the number of possible variables that can simultaneously vary.

Region I (Fig 1.5) corresponds to the low hydrogen concentration ( $C_H \ll 1$ ) at which hydrogen atoms dissolve randomly in the metal lattice forming a solid solution known as the  $\alpha$ -phase which has the same crystal structure as the metal. In this region, two components (metal and hydrogen) as well as two phases ( $\alpha$ -phase and hydrogen gas) exist. Using Equation (1.2):

$$F = 2$$

Thus, at constant temperature, hydrogen concentration increases with hydrogen pressure  $P_{H_2}$ . In this region, the concentration obeys Sievert's law ( $C_H \propto P_{H_2}^{1/2}$ ).

The concentration increases until the attractive H-H interaction becomes sufficiently important. This interaction is explained by the fact that the host metal lattice expands by hydrogenation, thus reducing the elastic energy for the introduction of hydrogen. When hydrogen reaches sufficient concentration, nucleation of the  $\beta$ -phase (ordered hydride phase) occurs as presented by region II of Figure 1.5.

In the region II, there is a transition from  $\alpha$  to  $\beta$  phase, i.e. growth of the hydride phase and the system now has three phases ( $\alpha$ -phase,  $\beta$ -phase and hydrogen gas) and two components (metal and hydrogen). The degree of freedom  $F$  is then equal to one. Therefore, in the two-phase region the hydrogen pressure is constant while hydrogen concentration increases. This constant pressure during the transition is called the plateau pressure of the PCI curve and it depends on temperature. With an increasing temperature, the plateau pressure increases but its width decreases (Fig 1.5) and at the critical temperature  $T_C$  no plateau exists.

Once the pure  $\beta$ -phase is reached, i.e.  $\alpha$ -phase is completely transformed to  $\beta$ -phase as shown in region III (Fig 1.5), an additional degree of freedom is restored and the further absorption of hydrogen would now require a notable increase in hydrogen pressure at which hydrogen enters into the solid solution into the  $\beta$ -phase.

A series of PCI curves at different temperatures enable the construction of a Van't Hoff plot as presented in the right side of Figure 1.5. It is used to determine experimentally the thermodynamic parameters of formation of a metal hydride by using the Van't Hoff relation given by:



$$\ln(P_{H_2}) = \frac{\Delta H}{RT} - \frac{\Delta S}{R} \quad (1.3)$$

where  $\Delta H$  is the enthalpy change during the formation of the hydride (transition  $\alpha$  to  $\beta$ ),  $\Delta S$  is the associated change in entropy,  $R$  is the gas constant and  $T$  is temperature.

The entropy change with hydride formation is mainly due to the loss of the standard entropy of hydrogen gas. Knowing that the standard entropy of hydrogen is  $S_0 = 130 \text{ J} \cdot \text{K}^{-1} \text{ mol}^{-1}$  at 100 kPa then, to a first approximation, the entropy change could be considered constant:  $\Delta S = -130 \text{ J} \cdot \text{K}^{-1} \text{ mol}^{-1} \text{ H}_2$ . The enthalpy  $\Delta H$  is a parameter that determines the stability of the metal hydride bonds, i.e. it measures the strength of metal-hydrogen bond.

The enthalpy of formation of the hydrides determines the amount of heat which is released during hydrogen absorption and consequently to be supplied in case of desorption.

According to Equation (1.3), the slope of the line obtained (Van't Hoff plot in right upper part of Fig 1.5) is  $\frac{\Delta H}{RT}$  while its y-intercept is  $-\frac{\Delta S}{R}$ .

In a BCC (body cubic centered) solid solution, the distribution of atoms on the lattice sites is random. These sites have different chemical and geometrical configurations and thus different energies. As a result, the interstitial sites that could be occupied by hydrogen are not equivalent. So, the heat of formation of hydrogen will be different for interstitial sites with different atomic surrounding and this will give rise to a sloping plateau. An example is given in Figure 1.6. This slope could change over the whole length of the plateau. It is attributed to compositional inhomogeneities.

In a PCI curve, the reversible capacity is the capacity that could be obtained in absorption/desorption process under practical conditions of temperature and pressure. The hydrogen capacity could be expressed in terms of atomic ratio  $H/M$  which is the number of hydrogen atoms stored for each metal atoms or, in weight percent wt % which is the weight of hydrogen stored over the weight of hydride phase.



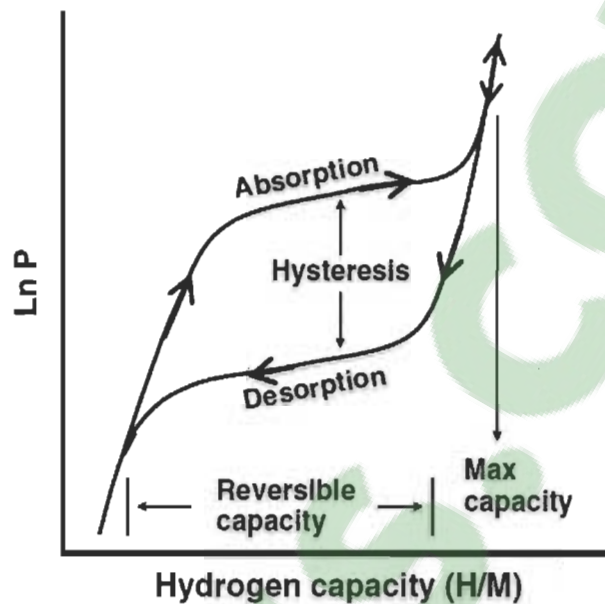


**Figure 1.6: Schematic presentation of sloping plateau, hysteresis and reversible capacity [18]**

The hysteresis (shown in Fig 1.6) between absorption and desorption pressures in PCI curves could be due to the difference in elastic and plastic energies resulting from creation of defects and dislocations in hydrogenation and dehydrogenation processes [19]. Reduction of hysteresis could be attained by heat treatment and by element substitution.

### 1.1.5 Activation process

The first hydrogenation is also called the activation process. The surfaces of metal alloys are generally covered with oxide layers whose thickness depend on the synthesis process. These layers act as a hydrogen barrier and should be broken for hydrogen to be in contact with the bare metal surfaces.

The activation process is usually performed at high hydrogen pressure and at high temperature. These conditions make it easier to force hydrogen through the oxide layer and this will offer a fresh metal surface for interaction with hydrogen.

## 1.2 Ti-V-Cr BCC solid solution

Ti-V-Cr BCC solid solution alloys are well known as promising hydrogen storage materials. They are widely studied considering their operating conditions close to normal temperature and pressure conditions and their reversible hydrogen capacity ( $> 2$  wt %) [20-23].

For the present investigation, by looking at a ternary phase diagram of the Ti-V-Cr system, a composition was selected. BCC structure is preferred for hydrogen storage rather than FCC (face cubic centered) and HCP (hexagonal close packed) structures because it has more interstitial sites in the lattice [24]. Moreover, diffusivity of hydrogen is higher in BCC structure [25].

One of the problems of Ti-V-Cr system is the slow and difficult activation process. Many approaches have been taken to overcome this drawback such as heat treatment and mechanical deformation.

Heat treatment is an approach that solves the activation problem. It is usually carried out at a high temperature (from  $500^{\circ}\text{C}$  to  $1000^{\circ}\text{C}$ ). The treatment breaks the oxide layers on a metal surface and improves the hydrogen sorption properties of as-cast alloys [26, 27]. However, this approach leads to additional cost on the industrial scale.

Mechanical deformation is another approach that has been used. Edalati et al. [28] found that in Ti-V BCC alloys processed by high pressure torsion, microstructural modifications were induced therefore introducing lattice defects and so enhancing hydrogen storage properties. However, the main drawback for mechanical deformation is the fact that it is difficult and expensive to scale-up [29].

## 1.3 Effect of a secondary phase

Recently, the addition of  $\text{Zr}_7\text{Ni}_{10}$  to the Ti-V-Cr system was found to drastically improve the activation process [30-33]. In these alloys, a specific microstructure is formed. The microstructure is made of a main BCC phase and a Zr and Ni rich secondary phase. The

secondary phase is considered to be acting as a gateway for hydrogen to enter into the main BCC phase [34].

In investigations done by Shashikala et al., where they tried to replace Ti by Zr in Ti-V-Cr system, they noticed the appearance of a secondary phase that is rich in Zr [35].

SEM analyses were done by Bibienne et al. on Ti-V-Cr system with many compositions doped with  $Zr_7Ni_{10}$  [30, 36]. According to their results, almost all zirconium was found in the secondary phase.

In the different system TiFe, Jain et. al demonstrated that addition of  $Zr_7Ni_{10}$  leads to easy activation [37]. Moreover, they tested the effect of Zr and they concluded that a better performance of TiFe alloy could be obtained by addition of Zr rather than  $Zr_7Ni_{10}$  [38].

#### **1.4 Objective of this research**

In section 1.2, we saw that activation by high temperature or by mechanical alloying could be time consuming and costly for the industry. Therefore, there is a need of a material that will be cheap and efficient for activation. From previous investigations, it was shown that adding  $Zr_7Ni_{10}$  helps the activation.

In this research, we picked the system  $Ti_{1.1}V_{0.9}Cr_{1.1}$  that was used by Miraglia et al. [32]. Instead of adding  $Zr_7Ni_{10}$  as Miraglia we decided to add only Zr.

We think that the addition of Zr in pure state could be sufficient for solving the activation problem as well as improving the performance of Ti-V-Cr system.

The effect of adding zirconium on hydrogen properties of Ti-V-Cr system was investigated. The microstructure and the crystal structure were studied in order to see if there is a relationship between microstructure and hydrogen storage properties of these materials.

## Chapter 2: Experimental Methods

This chapter presents the experimental techniques that were employed for the synthesis, characterization and evaluation of the hydrogen storage properties of  $\text{Ti}_1\text{V}_{0.9}\text{Cr}_{1.1} + x \text{ wt } \% \text{ Zr}$ . An arc melting furnace was used for synthesis of alloys. Hydrogen absorption kinetics were measured by a Sievert's type apparatus developed in our laboratory. The characterization of the samples has been performed by: Scanning electron microscopy (SEM), Energy Dispersive X-ray (EDX) and X-Ray powder diffraction (XRD).

Brief descriptions of the general principles of these techniques are presented in the following sections.

### 2.1. Arc Melting

Arc melting is a conventional and easy technique to prepare alloys with good reproducibility. Figure 2.1 shows the arc melting setup used in our laboratory.

The sample is placed in a copper crucible after mixing the desired stoichiometry. The system is pumped down via a rotary pump to remove air and then back filled with argon gas. Hence, melting is performed in argon atmosphere.

An electrically generated arc, between the crucible copper electrode and a tungsten electrode, causes fusion of the materials by Joule's effect. To ensure homogeneity, the obtained pellets were turned over and re-melted three times.



**Figure 2.1: Arc-melting furnace**

## **2.2 Characterization of materials**

### **2.2.1 Scanning Electron Microscopy (SEM)**

A SEM image is formed by a finely focused beam of energetic electrons scanning over the sample's surface area. The important feature of SEM is the 3-dimensional appearance of its image due to its large depth of field. SEM provides detailed high-resolution images of the sample. In addition, chemical information could be obtained by equipping the SEM system with an X-ray energy-dispersive spectrometer (EDX) [39].

The key components of SEM are: electron gun, electromagnetic lenses and detectors. Electrons are used due to their wave-particle duality. The high energy electrons generated by the electron gun are accelerated and focused on the sample using the lenses. The electrons interact with atoms in the sample at various depths as shown in Figure 2.2.

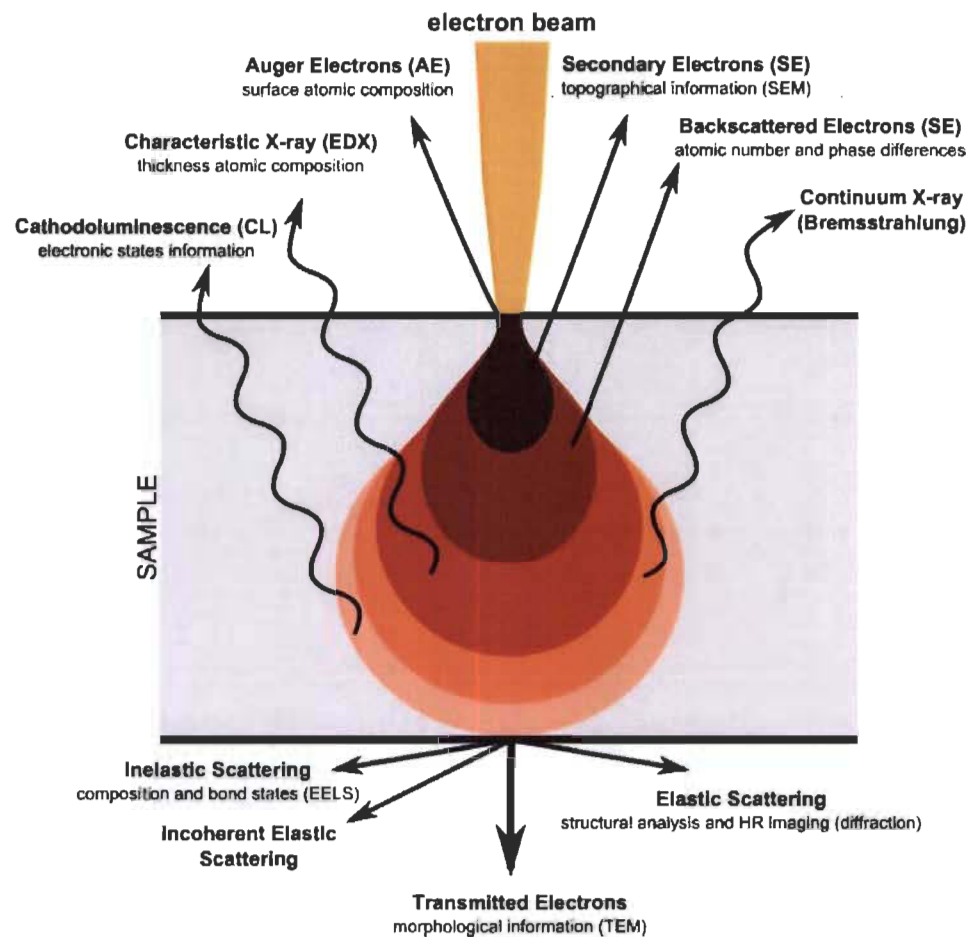


**Figure 2.2: Signals emitted from different parts of the interaction volume [40]**

This interaction results in the emission of secondary electrons “SEs” by inelastic scattering, in the reflection of high-energy electrons (so called back scattered electrons “BSEs”) by elastic scattering, and/or the emission of electromagnetic radiation as presented in Figure 2.3.



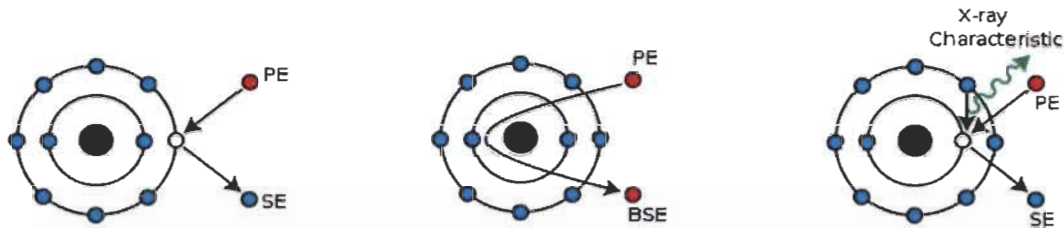


**Figure 2.3: Mechanisms of emission of secondary electrons, backscattered electrons, and characteristic X-rays from atoms of the sample [40]**

The secondary electrons “SEs” are emitted from atoms in the sample (mainly on the surface) which are deflected at small angles. The image obtained by the SEs gives the morphology of the sample.

Back scattered electrons “BSEs” are the incident electrons reflected or back scattered by atoms in the sample (penetrate deeper) which are deflected at large angles and with small energy loss. This scattering depends on the atomic number  $Z$  of the elements.

The higher the atomic number the more backscattered electrons thus a brighter image compared to elements with a lower atomic number. So, the areas that contain heavier elements will be easier to see than areas with lighter ones.

### **2.2.2 Energy Dispersive X-ray spectroscopy (EDX)**

EDX is a technique that provides elemental analysis alongside the high-resolution imaging of SEM. With these two techniques combined, we obtain not only information concerning the morphology of the sample, but also elemental information, in the form of maps and images of surfaces [41].

EDX uses X-rays emitted from the sample when the SEM electron beam hits the surface. These incoming electrons eject an electron from the atoms of the sample’s surface creating a hole. This hole is then filled by an electron from a higher shell. As the electron falls to a lower energy shell a photon is ejected. The number and energy of the X-rays emitted from the sample is measured by an energy-dispersive spectrometer.

These emitted X-rays due to the energy difference between the higher and the lower energy shells are directly correlated to the atomic structure of the emitting element [42]. The energy of these X-rays is used to identify the elements and provides information about their abundance.

### 2.2.3 X-Ray Diffraction

X-ray diffraction (XRD) is a technique used for the characterization and identification of crystalline phases in a material.

When a crystal is illuminated by an X-ray beam with wavelength comparable to the interatomic distances of the crystal lattice, a constructive interference between elastically scattered X-ray beams occurs at the Bragg's angle. Bragg's law (Figure 2.4) is expressed as:

$$2d_{hkl}\sin\theta_{hkl} = n\lambda$$

Where,  $d_{hkl}$  is the interplanar distance between two crystallographic planes in the crystal,  $\theta_{hkl}$  is the angle between the incident ray and scattering planes where the diffraction peak is observed (Bragg's angle),  $n$  is an integer number (order of reflection), it is normally equal to 1 and  $\lambda$  is the wavelength of the X-rays.

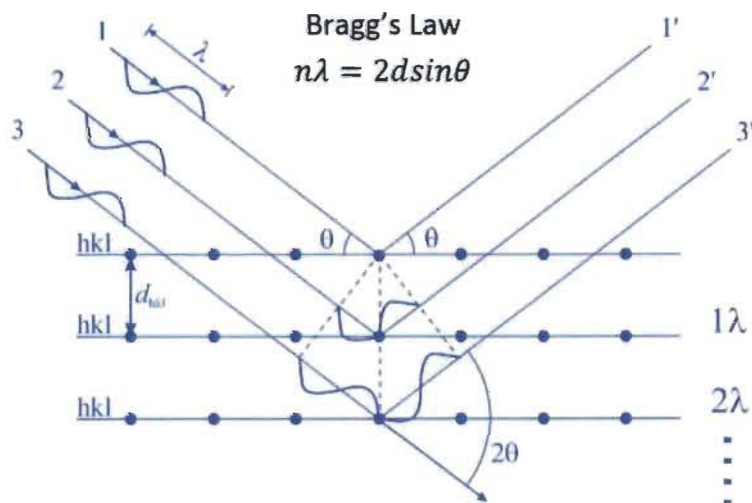


**Figure 2.4: Diffraction of incident X-rays from the family of parallel atomic planes [43]**



The interplanar distance  $d_{hkl}$  is a function of the Miller indices ( $hkl$ ) and the lattice parameters of the crystal lattice where ( $hkl$ ) represents the different crystallographic planes. Therefore  $d_{hkl}$  is dependent on the crystal structure.

A diffraction pattern is typically in the form of a graph of the diffraction angle (or interplanar spacing  $d_{hkl}$ ) versus the intensity of diffracted beam.

Each of these unique patterns can act as an empirical “fingerprint” for the identification of the present phases, by comparing them with patterns in the International Powder Diffraction File(PDF) database compiled by the Joint Committee for Powder Diffraction Standards (JCPDS) [44].

As a result, identification of the phases present is possible, but also a quantitative estimation of these phases could be made by the Rietveld method.

The Rietveld method is a whole-pattern fitting least squares refinement technique. This refinement can be performed on the pattern using a software like GSAS or Full-prof. The crystallographic parameters such as lattice parameters of the unit cell, size and strain of the crystallites as well as the position of the atoms and the phases abundance can be evaluated.

Figure 2.5 shows the Bruker D8 advance diffractometer with a Bragg-Brentano configuration, used in our laboratory.



**Figure 2.5: Bruker D8 advance X-Ray diffractometer**

### 2.2.4 Sievert's Apparatus

A Sievert-type experimental apparatus allows the study of the hydrogen absorption and desorption kinetics as well as the determination of the pressure–composition ( $P$ – $C$ ) diagram of the material–hydrogen system [45].

In our laboratory, a homemade Sievert-type hydrogen titration apparatus was used. This apparatus is made of a series of connecting pipes, valves and pressure gauges, as shown in Figure 2.6.

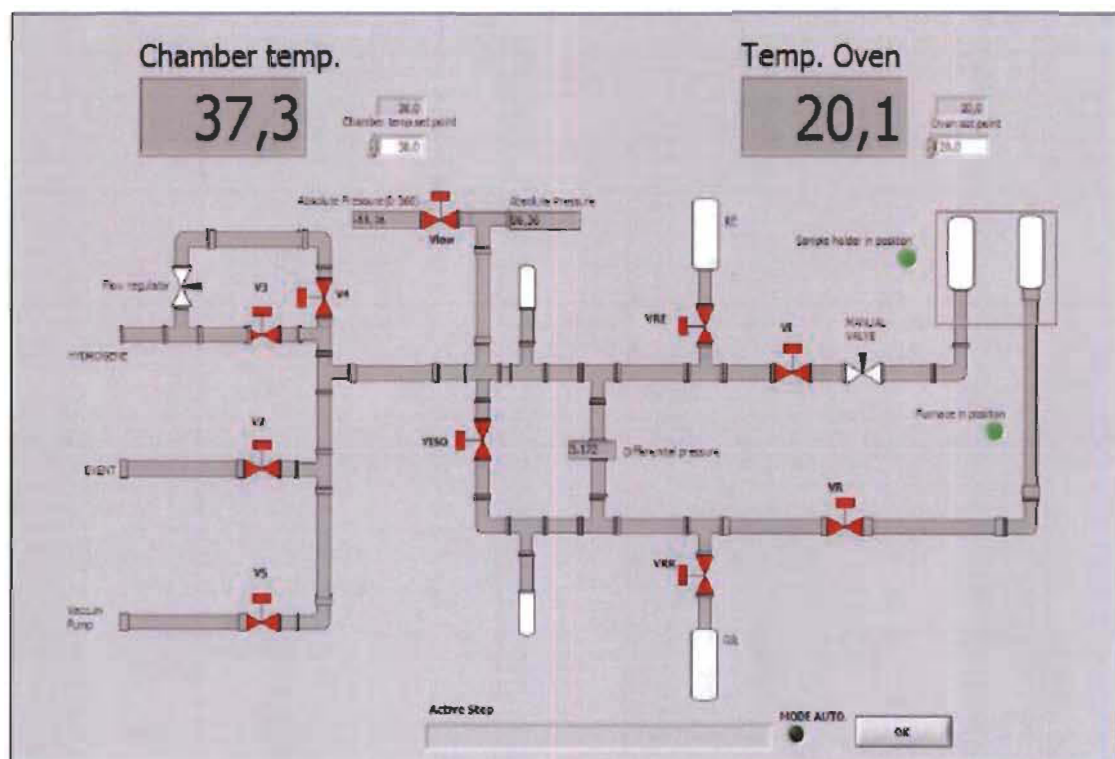


**Figure 2.6: Schematic of the hydrogen titration apparatus**

The volume of each component of the apparatus was accurately measured.

The pipes are connected to a hydrogen inlet, an exhaust outlet, an outlet attached to a vacuum pump, a reference side and a sample side that are separated by a differential pressure gauge. The reference and samples sides have identical volumes. The sample side pressure is measured relative to the reference side pressure by means of the differential pressure gauge.

By knowing the volume of each component, the amount of hydrogen absorbed/desorbed could be determined using the equation of state of hydrogen. The equation of state of hydrogen (considered a real gas) can be expressed, by virial expansion of the second order (this is sufficient for the pressure range used in this research), as:

$$PV = nRT(1 + \frac{B}{V}) \quad (2.1)$$

where P is the hydrogen pressure, V is the volume filled by hydrogen, n is the number of moles of hydrogen, R is the ideal gas constant (8.314 J. mole<sup>-1</sup>K<sup>-1</sup>), T is the temperature of the sample holder and B is the second virial coefficient and is temperature dependent. One can find the value of B in the reference [46].

Knowing that the volume of the apparatus is constant and the experiment is done at constant temperature, then the number of moles of H atoms absorbed by the sample is:

$$\Delta n = 2 \frac{V \Delta P}{RT(1 + \frac{B}{V})} \quad (2.2)$$

Where  $\Delta P$  is the pressure drop and the factor 2 corresponds to H atoms absorbed. This factor comes because the equation of state of gas is established for H<sub>2</sub>.

The percentage of mass of H atoms absorbed by the sample is calculated using the equation:

$$\% \text{ absorbed } H = \frac{\text{mass } H}{\text{mass}(\text{sample}+H)} \quad (2.3)$$

### 2.3 Synthesis and characterization of materials

In the present study, the following alloys were synthesized: Ti<sub>1</sub>V<sub>0.9</sub>Cr<sub>1.1</sub> + x wt % Zr with x=0, 2, 4, 8 and 12. The synthesis was done using an arc-melting furnace. The raw materials were purchased from Alfa-Aesar (Ward Hill, MA, USA) and had the following purities: Ti sponge (99.95%), V pieces (99%), Cr pieces (99%) and Zr sponge (99.95%). They were mixed at the desired stoichiometry and melted together under argon atmosphere. A current of intensity 40 Amperes was selected for synthesis of all samples.

Since these elements have similar melting points (melting points for Ti, V, Cr and Zr are 1668°C, 1910°C, 1907°C and 1855°C respectively), their melting was easy with no mass loss found after the melting.

Microstructure and chemical analysis were performed using a JEOL-JSM 5500 scanning electron microscopy equipped with an EDX apparatus from Oxford Instruments. For this analysis, the pellet was placed for one day in epoxy and then it was polished in steps by silicon carbide (SiC) abrasive grinding papers. It was grinded from 400 grit to 2400 grit sizes in order to get a surface like mirror. The used magnifications for the SEM images were of the order of 250X to 2500X. The percentage of different phases was analyzed by ImageJ software.

For kinetic and XRD measurements, each pellet after synthesis was hand crushed, using a steel mortar and pestle in an argon-filled glovebox. Crushing in air was performed only for the air exposed sample.

The powdered sample was filled without sieving into a sample holder. After loading the sample holder into the hydrogen titration apparatus, it was kept under vacuum for one hour at room temperature before exposing it to hydrogen. The temperature was regulated by a thermostatic bath. The kinetic measurements were performed under 2000 kPa of hydrogen and at room temperature (25°C).

The crystal structure was determined by powder XRD on a Bruker D8 focus apparatus with Cu K $\alpha$  radiation ( $\lambda_{K\alpha} = 1.5406 \text{ \AA}$ ). The angle of detection ranges from 30° to 110° for each sample. Lattice parameters were evaluated by Rietveld refinement of the X-ray patterns using Topas software. In order to keep the hydride phase, the absorption experiment was stopped after reaching full hydrogenation and the pressure kept at one bar of hydrogen.

## **Chapter 3: Microstructure and hydrogen storage properties of $\text{Ti}_1\text{V}_{0.9}\text{Cr}_{1.1}$ alloy with addition of x wt % Zr (x = 0, 2, 4, 8, and 12)**

### **3.1 Introduction**

In this chapter, we report our investigation of the effect of adding zirconium on the microstructure of  $\text{Ti}_1\text{V}_{0.9}\text{Cr}_{1.1}$  BCC alloy. Zirconium was added with the following percentages by weight: 2, 4, 8 and 12. The alloys  $\text{Ti}_1\text{V}_{0.9}\text{Cr}_{1.1} + x$  wt % Zr (x = 0, 2, 4, 8, and 12) were prepared by mixing all the constituent elements together in an arc melting furnace.

The impact of microstructure on the first hydrogenation was studied. The crystallographic parameters of all alloys before and after hydrogenation were determined. We will discuss how the amount of zirconium affects the relative abundance of secondary phase. Also, the first hydrogenation of a sample exposed to air was measured.

### **3.2 Results and discussions**

#### **3.2.1 Microstructure Analysis**

Figure 3.1 shows the backscattered electron micrographs of:  $\text{Ti}_1\text{V}_{0.9}\text{Cr}_{1.1} + x$  wt % Zr alloys where x = 0, 2, 4, 8, and 12. It is clear that the microstructure changes with x. Pure  $\text{Ti}_1\text{V}_{0.9}\text{Cr}_{1.1}$  (Figure 1a) shows a network of black areas structure.

Even with a slight doping of Zr (x = 2), a bright secondary phase appears. This could reveal that the bright phase is rich in Zr because the brightness indicates an element with a high number of electrons.

All the zirconium-containing alloys were found to be multi-phase: a matrix phase and a bright phase. Dendrites appeared from x = 8 and were clearly observed for x = 12. It is seen that more Zr leads to higher secondary phase abundance.

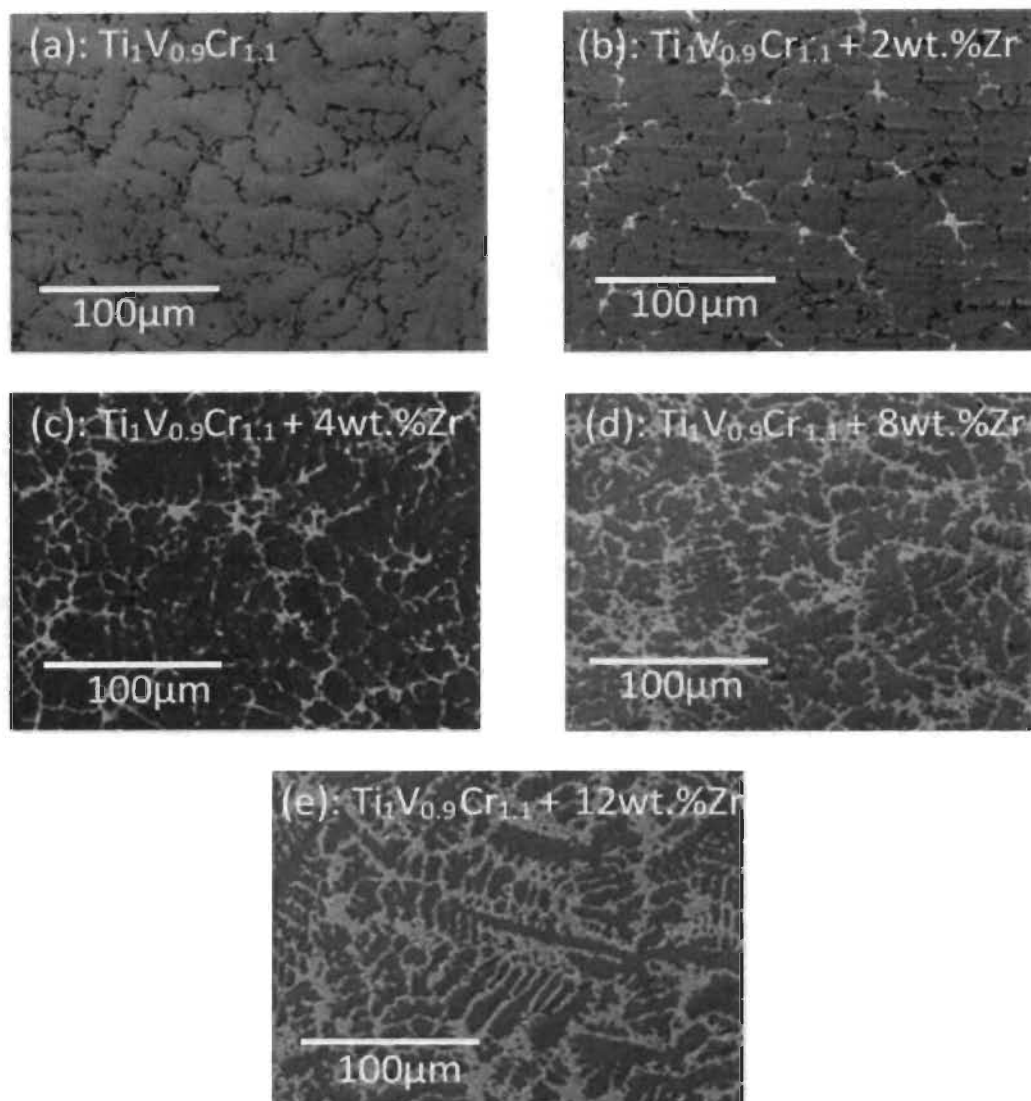


**Figure 3.1: Backscattered electrons (BSE) micrographs of:  $\text{Ti}_1\text{V}_{0.9}\text{Cr}_{1.1} + x \text{ wt \% Zr}$  with  $x = 0$  (a), 2 (b), 4 (c), 8 (d) and 12 (e)**

By using ImageJ software, the bright phase surface areas were measured. The percentage of the bright areas are 0, 4, 12, 26, and 35 respectively for  $x = 0, 2, 4, 8$ , and 12. It shows that, as the amount of Zr increases, the bright phase surface area is getting bigger.

To determine the chemical composition of the alloys, EDX measurements were performed. Table 3.1 shows the bulk measured atomic abundance compared to the nominal composition for all alloys studied. We see that the bulk measured composition agrees with the nominal one in all cases. This was expected because all these elements have similar melting points.



**Table 3.1: Bulk atomic abundance: nominal and as measured by EDX of:  $\text{Ti}_1\text{V}_{0.9}\text{Cr}_{1.1} + x$  wt % Zr alloys for  $x = 0, 2, 4, 8$  and  $12$ . Error on the last significant digit is indicated in parentheses**

Sample		Ti (at %)	V (at %)	Cr (at %)	Zr (at %)
<b>x=0</b>	Nominal composition	33	30	37	0
	Measurement	34.0(2)	29.8 (3)	36.2 (3)	0.0
<b>x=2</b>	Nominal composition	32.6	29.7	36.6	1.1
	Measurement	32.8 (2)	29.4 (2)	36.4 (3)	1.4 (1)
<b>x=4</b>	Nominal composition	32.3	29.3	36.2	2.2
	Measurement	34.0 (3)	28.2 (1)	35.2 (3)	2.6 (1)
<b>x=8</b>	Nominal composition	31.6	28.7	35.4	4.3
	Measurement	32.3 (2)	27.7 (2)	34.5(3)	5.5 (1)
<b>x=12</b>	Nominal composition	30.9	28.1	34.7	6.3
	Measurement	31.7 (2)	26.2 (2)	33.9 (2)	8.2 (1)

Figure 3.2 presents BSE micrographs with elemental mapping for  $\text{Ti}_1\text{V}_{0.9}\text{Cr}_{1.1} + x$  wt % Zr alloys where  $x = 0$  (a), 2 (b), 4 (c), 8 (d) and 12 (e). These micrographs show that the alloys are made of a main phase thereafter called matrix and indicated by point number 1, bright secondary phases (points 2 and 3) and a dark phase (point 4).

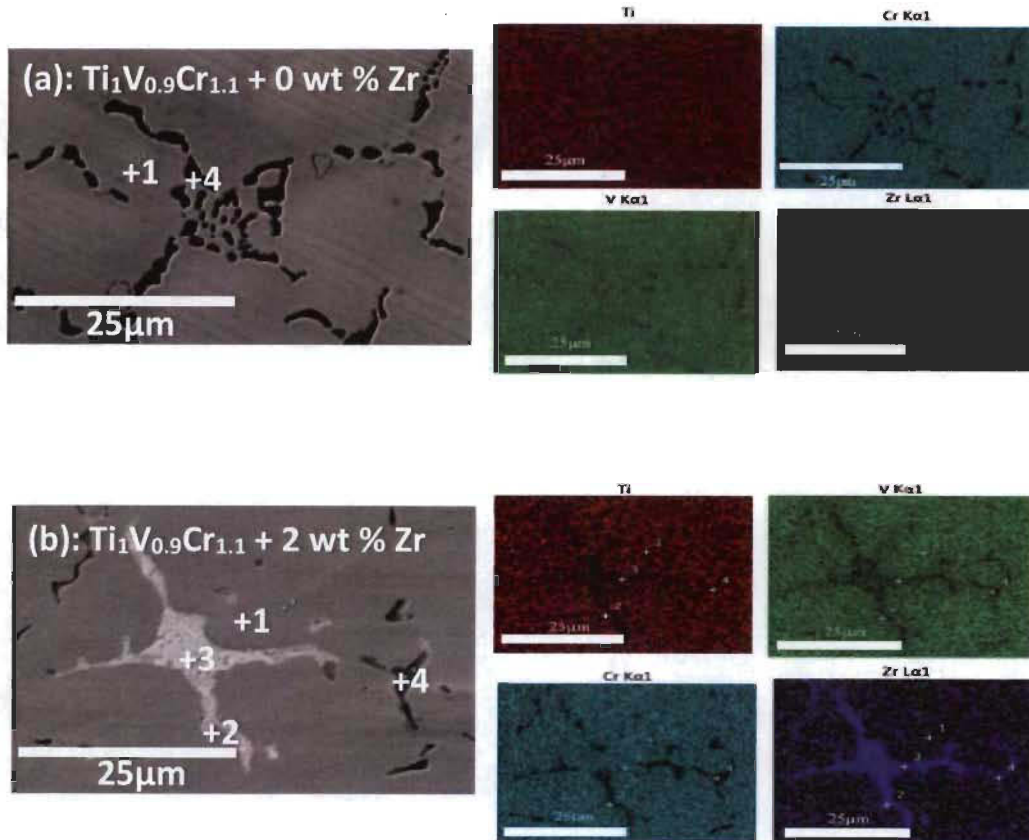
Fig 3.2a displays the microstructure of the undoped sample and it can be seen that it is just formed of a matrix and some dark phase. The dark phase is about few microns in size. The EDX mapping indicates that the dark phase is Cr and V depleted.

By adding 2 wt % Zr (Fig. 3.2b), a bright secondary phase appears. Close inspection, reveals that the brightness has two shades, region 3 being brighter than region 2. The EDX mapping shows that the secondary phases are Zr rich and V depleted. In this alloy, dark phase is less abundant than for the bare alloy.

At 4 wt % addition of Zr (Fig 3.2c), the quantity of secondary phase seems almost the same as for  $x=2$  and Zr is mainly in the secondary phase. Also, the secondary phase has two shades. The size of dark phase is getting smaller.

For 8 wt % Zr (Fig 3.2d), more secondary phase appears. It is clearly shown that the secondary phase is Zr and Cr rich and V depleted. There is no dark phase.

By adding more Zr (12 wt %), even more secondary phase appears (Fig 3.2e) and the dark phase disappears. It could be observed that the secondary phase is Zr and Cr rich and poor in V. Close inspection of Fig 3.2b, c, d and e indicates that region 2 is usually on the edge of the bright surfaces while region 3 is more in the centre. Thus, it seems that the secondary phase 1 is bridging the secondary phase 2 with the matrix.





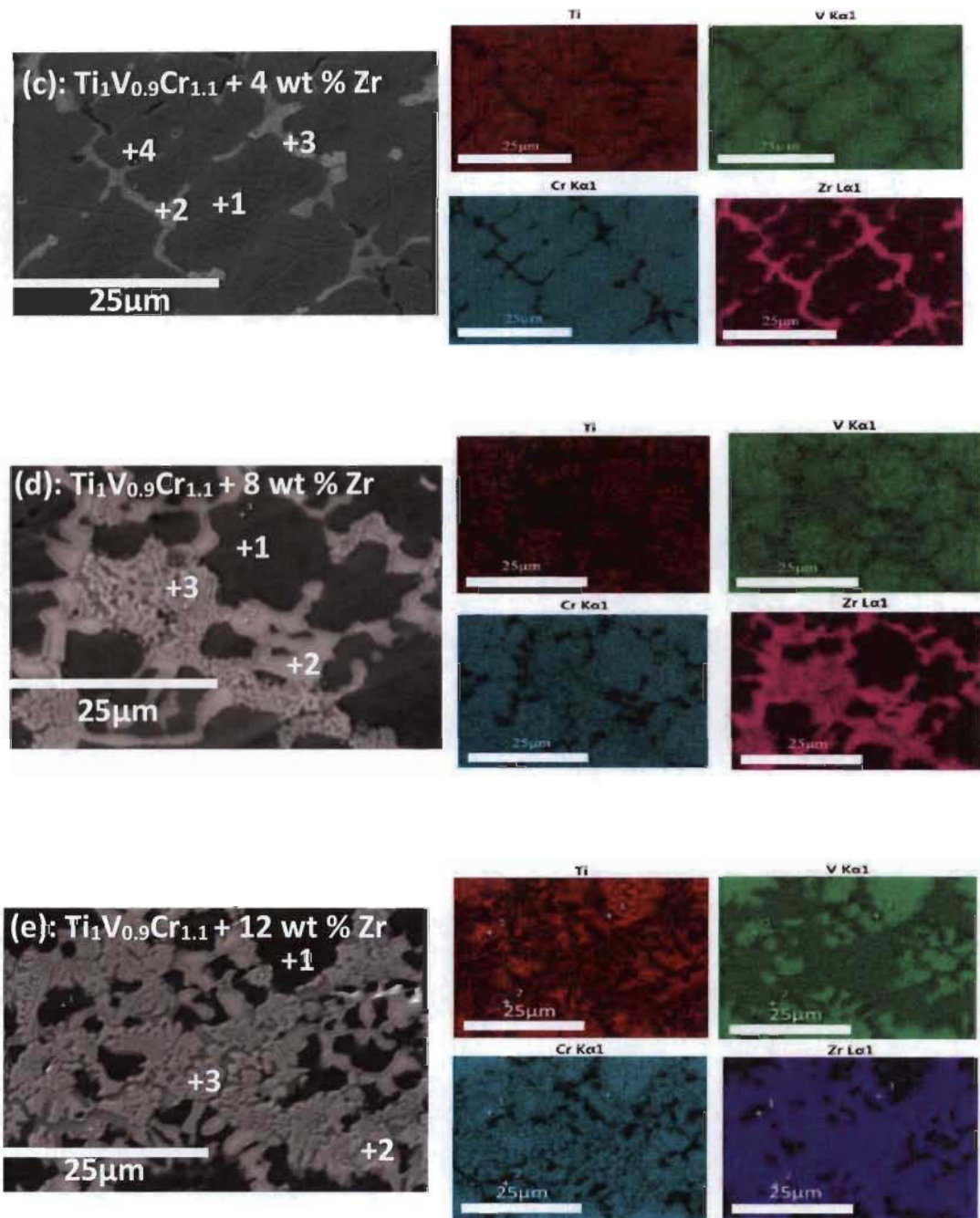


**Figure 3.2: Backscattered electrons micrographs of:  $\text{Ti}_1\text{V}_{0.9}\text{Cr}_{1.1} + x \text{ wt } \% \text{ Zr}$  alloys with elements mapping where  $x=0$  (a), 2 (b), 4 (c), 8 (d) and 12 (e)**

A quantitative analysis was done by EDX measurements at the specific locations presented in Fig 3.2. Chemical composition of regions 1, 2, 3 and 4 are listed in the Tables

3.2 to 3.5 respectively. Table 3.2 presents the composition of the matrix (point 1) for all alloys.

**Table 3.2: EDX analysis showing the elemental composition of the matrix (point 1) of:  $\text{Ti}_1\text{V}_{0.9}\text{Cr}_{1.1} + x$  wt % Zr alloys for  $x = 0, 2, 4, 8$  and  $12$ . Error on all values is  $0.1$  at %**

Sample	Ti (at %)	V (at %)	Cr (at %)	Zr (at %)
x=0	27.8	33.8	38.4	0.0
x=2	27.4	33.4	38.9	0.3
x=4	25.8	35.0	38.9	0.3
x=8	29.3	31.6	38.2	0.9
x=12	28.5	31.7	38.9	0.9

From this table, it can be seen that the matrix is a Ti–V–Cr alloy with inclusion of only a very small amount of Zr ( $<1$  at %). The matrix composition does not significantly change when more zirconium is added.

On average, the atomic composition of the matrix is  $\text{Ti}_{0.84}\text{V}_1\text{Cr}_{1.2}\text{Zr}_{0.03}$  which is quite different than from the nominal value. The main difference is that, compared to the nominal composition, the titanium proportion is reduced, the vanadium amount increased. The chromium abundance is almost the same as the nominal one.

As the amount of zirconium was very small in the matrix, it can be expected that zirconium will be mainly confined in the secondary phases. This can be seen in Tables 3.3 and 3.4 that show the atomic composition of the two secondary phases. Secondary phase one (point 2) is rich in Ti and Zr while secondary phase two (point 3) has a relatively high content of the four elements.

**Table 3.3: EDX analysis showing the elemental composition of the secondary phase 1 (point 2) of  $\text{Ti}_1\text{V}_{0.9}\text{Cr}_{1.1} + x$  wt % Zr alloys for  $x = 0, 2, 4, 8,$  and  $12$**

Sample	Ti (at %)	V (at %)	Cr (at %)	Zr (at %)
$x = 2$	64.0	7.0	6.2	22.8
$x = 4$	64.0	6.7	6.2	23.1
$x = 8$	58.3	6.8	4.6	30.3
$x = 12$	55.8	7.2	5.1	32.0

From Table 3.3, we see that the secondary phase 1 (point 2) is close to composition  $\text{Ti}_{1.9}\text{V}_{0.2}\text{Cr}_{0.2}\text{Zr}_{0.7}$  for  $x = 2$  or  $4$  and to composition  $\text{Ti}_{1.7}\text{V}_{0.2}\text{Cr}_{0.2}\text{Zr}_{0.9}$  for  $x = 8$  and  $12$ .

To our knowledge, there are no quaternary alloys that have a stoichiometry close to these. Comparing these two compositions, it could be seen that when  $x$  is higher than  $8$  it seems that there is substitution of Ti by Zr (Zr is getting up by  $0.2$  and Ti is going down by  $0.2$ ) while V and Cr abundances stayed the same. It can be an indication that Ti and Zr are sitting on the same crystallographic site.

Table 3.4 shows the composition of secondary phase 2 (point 3). This phase has an almost constant composition  $\text{Ti}_{1.0}\text{V}_{0.4}\text{Cr}_{1.1}\text{Zr}_{0.5}$  and also has a high zirconium content but here chromium is the most abundant element. Contrary to secondary phase 1, the composition of this phase does not vary significantly with increasing  $x$ .

**Table 3.4: EDX analysis showing the elemental composition of secondary phase 2 (point 3) of:  $\text{Ti}_1\text{V}_{0.9}\text{Cr}_{1.1} + x$  wt % Zr alloys for  $x = 0, 2, 4, 8$ , and  $12$**

Sample	Ti (at %)	V (at %)	Cr (at %)	Zr (at %)
$x = 2$	33.7	12.3	38.0	16.0
$x = 4$	32.8	12.3	37.9	17.0
$x = 8$	32.8	15.5	33.6	18.1
$x = 12$	28.5	14.8	36.5	20.2

Chemical composition of the black phase (point 4) was measured and the results are reported in Table 3.5

**Table 3.5: EDX analysis showing the elemental composition at point 4 of:  $\text{Ti}_1\text{V}_{0.9}\text{Cr}_{1.1} + x$  wt % Zr alloys for  $x = 0, 2$ , and  $4$**

Sample	Ti (at %)	V (at %)	Cr (at %)	Zr (at %)
$x = 0$	87.7	7.0	5.3	0.0
$x = 2$	88.2	3.3	2.0	6.5
$x = 4$	79.6	6.8	5.6	8.0

It is evident that the black areas are titanium precipitates. The amount of precipitation tends to decrease with increasing Zr content and for 8 and 12 wt % of Zr there are no Ti-precipitates.

### 3.2.2 Structural Characterization

Figure 3.3 presents the XRD pattern of all the studied samples in the as-cast state. The major diffraction peaks of all as cast alloys can be identified as BCC phase (space group  $Im-3m$ ). Small peaks appeared as the zirconium doping increases. These peaks are surely related to the secondary phases. Due to the smallness of the peaks and their relatively small numbers, indexing them is difficult.

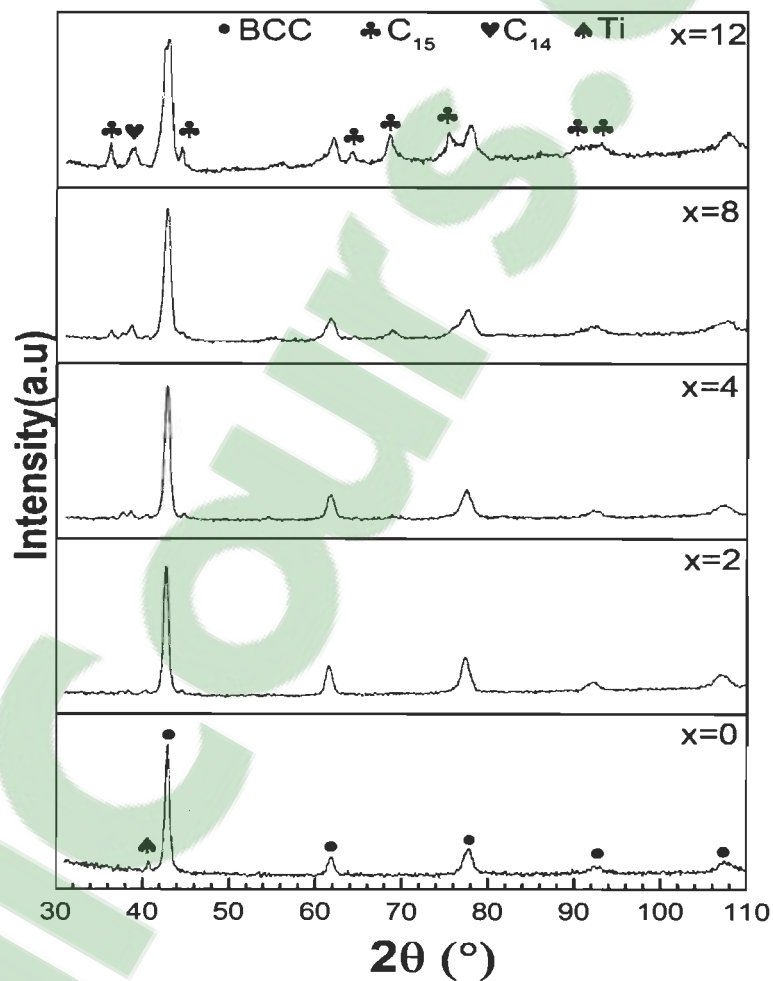


**Figure 3.3:** X-ray diffraction patterns of as cast:  $\text{Ti}_1\text{V}_{0.9}\text{Cr}_{1.1} + x \text{ wt \% Zr}$  alloys with  $x = 0, 2, 4, 8, \text{ and } 12$

As demonstrated by Akiba and Iba, Laves phases could be closely related to BCC alloys [20]. Laves phases are well known intermetallic phases that crystallize in three different structures: a cubic  $\text{MgCu}_2$ -type (Space group  $Fd-3m$ ), a hexagonal  $\text{MgZn}_2$ -type (space

group  $P6_3/mmc$ ), or a hexagonal  $MgNi_2$ -type (Space group  $P6_3/mmc$ ). Following the *Strukturbericht* nomenclature, these phases will be thereafter respectively designated C15, C14, and C36. In the specific case of Ti–V–Cr BCC alloys, it was also shown by Bellon et al. [47] that when zirconium is substituted for vanadium in these alloys there is the appearance of a C15 Laves phase.

We analyzed our diffraction patterns by Rietveld's refinement. The obtained crystal parameters and the abundance of each phase in all samples are shown in Table 3.6.

**Table 3.6: Crystal parameters and abundance of each phase in as cast:  $Ti_{1.1}V_{0.9}Cr_{1.1} + x$  wt % Zr alloys for  $x = 0, 2, 4, 8$ , and  $12$ . Error on the last significant digit is indicated in parentheses**

Sample	Phase	Lattice parameter (Å)	Crystallite size (nm)	Phase abundance (%)	Bright Area abundance (%)
x=0	BCC	3.0379 (9)	24 (2)	97 (3)	0
	Ti	a=2.961 (4)	13 (2)	3 (3)	
		c=4.773 (1)			
x=2	BCC	3.0479 (5)	22 (1)	92 (2)	4
	C15	7.172 (7)	14 (7)	2 (1)	
	C14	a=5.903 (9) c=7.26 (2)	8 (2)	6 (2)	
x=4	BCC	3.0470 (7)	23 (2)	89 (3)	12
	C15	7.153 (5)	20 (8)	3 (1)	
	C14	a=5.935 (1) c=8.09 (4)	5 (1)	8 (3)	
x=8	BCC	3.0452 (1)	38 (9)	68 (5)	26
	C15	7.180 (5)	6 (1)	21(4)	
	C14	a=5.849 (7) c=8.109 (2)	6 (1)	11 (2)	
x=12	BCC	3.0310 (1)	8 (3)	66 (4)	35
	C15	6.099 (7)	10 (1)	22 (2)	
	C14	a=5.815 (2) c=8.01 (1)	3 (1)	12 (2)	

In these refinements, we tried to index the secondary phases' peaks with Laves phases. It was found that the peaks could be indexed by using two Laves phases, namely the C15

and C14 phases. Tentatively, the C14 phase was assigned to the composition  $\text{Ti}_{1.9}\text{V}_{0.2}\text{Cr}_{0.2}\text{Zr}_{0.7}$  (secondary phase 1) and the C15 phase to the composition  $\text{Ti}_{1.0}\text{V}_{0.4}\text{Cr}_{1.1}\text{Zr}_{0.5}$  (secondary phase 2).

However, as it is difficult to distinguish between Ti, V, and Cr by X-ray diffraction the exact assignment could be only done by using neutron diffraction. Also, the problem with these compositions is that the ratio A/B is not 2 as it should be for C14 and C15 phases.

For these reasons, it should be stressed that the indexing of C14 and C15 is tentative and more experiments are needed in order to have the definitive crystal structure of the secondary phases. We are now undertaking neutron experiments and these will be reported in a future paper.

It could be concluded that using two Laves phases for fitting the secondary phase peaks confirm the finding of electron microscopy where two different secondary phases were found.

It should also be pointed out that, on Figure 3.3 only the main peaks of C14 and C15 have been indexed. As these two phases have small abundances, only the main peaks are showing in the diffraction patterns and indexing all possible peaks would have confused the reader, especially for overlapping peaks that are so small that they are undistinguishable from the background.

Referring to Table 3.6 at which the phase abundances are presented for all studied alloys, the total abundance of C15 + C14 phases roughly matched the abundance measured with ImageJ software.

### 3.2.3 Activation process

The first hydrogenation (activation) of as-cast  $\text{Ti}_{1.9}\text{V}_{0.9}\text{Cr}_{1.1} + x \text{ wt } \% \text{ Zr}$  alloys was performed at room temperature under a hydrogen pressure of 2 MPa after the alloys had been crushed in argon. Results are presented in Figure 3.4.



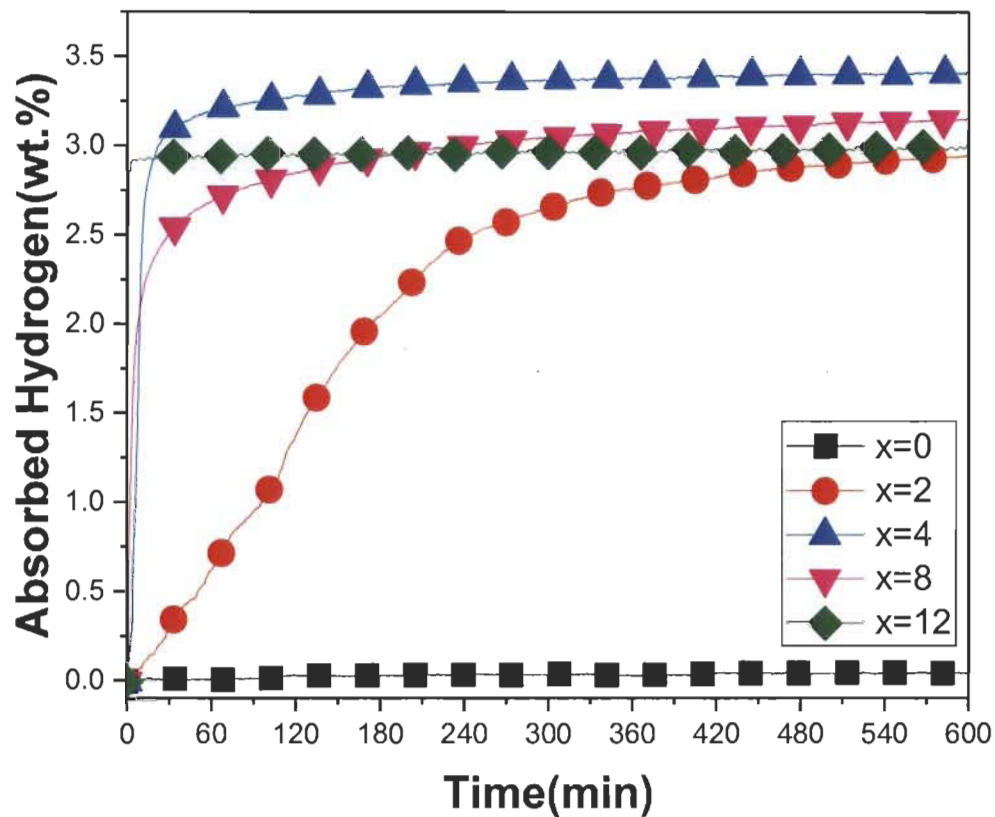


**Figure 3.4: Activation curves of:  $\text{Ti}_1\text{V}_{0.9}\text{Cr}_{1.1} + x$  wt % Zr for  $x = 0, 2, 4, 8$ , and 12 at room temperature under 2 MPa of hydrogen**

The first hydrogenation for  $x = 0$  is practically impossible. This sample did not absorb hydrogen even after 900 min of hydrogen exposure. Adding only 2 wt % of Zr to the alloy resulted in a good hydrogen uptake, but the full hydrogenation still took about 10 h. Increasing  $x$  value to 4 wt % had the effect of greatly enhancing the kinetics and full hydrogenation was achieved after 150 min. Further increase of zirconium content slightly improved the kinetics but the total capacity decreased. Among all doped samples, the one with 12 wt % Zr has the fastest activation kinetics, reaching maximum capacity within 3 min. For hydrogen storage purposes, the optimum amount of zirconium seems to be 4 wt %. However, even if the capacity slightly decreases with addition of more zirconium, the decrease in capacity is not very important.



In the alloy with 12 wt % of Zr the secondary phases comprise between 35 wt % (as measured from SEM images) and 34 wt % (as determined from Rietveld refinement).

Taking the low estimation of 34 wt %, if these secondary phases do not absorb hydrogen, and assuming that pure BCC absorbs about 4 wt % of hydrogen, we should expect a capacity of about 2.7 wt % which is clearly not the case. The measured capacity can not be explained by the presence of the BCC alloy itself. Thus, we have evidence that, at least one of the secondary phases absorbs hydrogen.

Nonetheless, this then raises the question of the kinetic curves. Except for the 2 wt % Zr alloy, all activation curves do not show any kinks or slope change. This is the signature of a single-phase alloy which is evidently not the case here. However, it has been shown by Akiba and Iba [20] that the BCC Laves phase related alloys could actually be formed by a BCC phase and a Laves phase and still display a single-phase behaviour upon hydrogen absorption. It seems to be the case in the present system.

As the alloys with Zr addition have a multiphase structure, it is clear that interphase boundaries probably play a role in the activation. Similar investigation in other systems seems to point that way [48].

Nanocrystallinity is also well known to enhance hydrogenation/dehydrogenation kinetics [23]. However, in the present case it is not the main factor as evidenced by Table 3.6. From this table, we see that the samples with  $x=2$  and  $x=4$  have almost the same crystallite size but their activation curve is drastically different.

Moreover, the sample with  $x=8$  has a larger crystallite size but the hydrogenation is faster. Therefore, nanocrystallinity alone could not explain the behaviour of this system. Dislocations and defects could lead to a faster first hydrogenation in metal hydrides and this was shown for cold rolled alloys [49, 50].

Another explanation for the quick activation of alloys with zirconium addition may be stability of the FCC hydride. As the matrix of the Zr-containing alloys has a stoichiometry different from the nominal value and also, taking into account the fact that the BCC alloy contains some zirconium, it may well result in some change of the formation enthalpy of the FCC hydride phase.

Obviously, thermodynamics should play a role in the improvement of kinetics. From the EDX measurements, we saw that the amount of Zr in the BCC matrix is small, then we don't expect a big change of thermodynamics of our alloys compared to the work of Miraglia [32]. However, to have a complete understanding of  $\text{Ti}_1\text{V}_{0.9}\text{Cr}_{1.1}$  alloys with Zr addition, and to determine the effect of thermodynamic change in the variation of kinetics, the pressure-composition curves and associated Van't Hoff plot should be made. Unfortunately, this type of investigation is too time-consuming to be within the scope of the present thesis.

#### **3.2.4 XRD patterns after Hydrogenation**

In order to study the crystal structure of the hydride phase in this set of experiments, the absorption experiment was stopped after reaching full hydrogenation and thereafter the hydrogen pressure was lowered to 1 bar. No vacuum was applied to the sample so that desorption does not occur during the sample holder removal. In separate tests, we exposed the samples to a pressure of 10 kPa and no desorption was noticed. Figure 3.5 shows X-ray diffraction patterns of all alloys after first exposure to hydrogen.

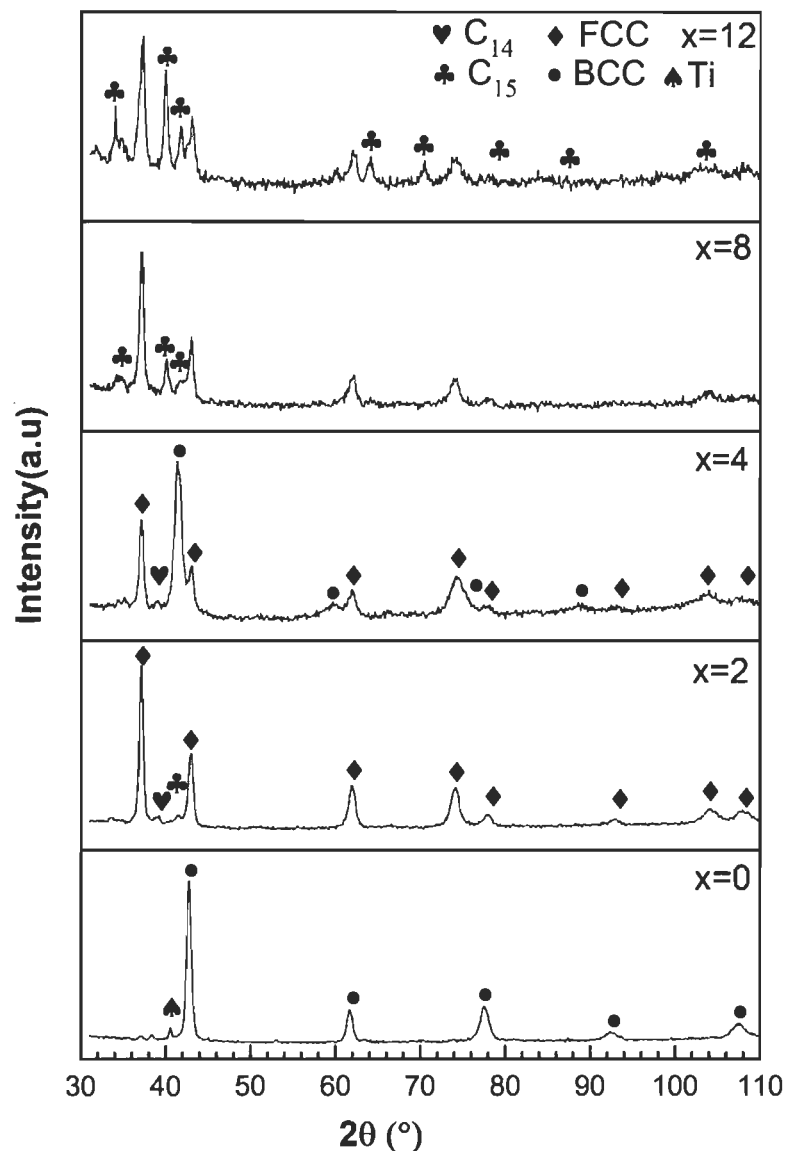


**Figure 3.5: X-ray diffraction patterns of:  $\text{Ti}_1\text{V}_{0.9}\text{Cr}_{1.1} + x$  wt % Zr alloys in the hydrogenated state for  $x = 0, 2, 4, 8$ , and  $12$**

We see that for  $x = 0$ , the structure is BCC. For  $x = 2$ , the crystal structure is essentially FCC which is usually the crystal structure adopted by a fully hydrided BCC alloy. The FCC phase is also seen in the patterns for  $x = 4, 8$ , and  $12$  but there are clearly other phases present. Indexation of the supplementary peaks is helped by doing a Rietveld's refinement. Even if in a Rietveld refinement prior knowledge of the phase present is mandatory, we could use this technique to first fit the patterns by using the known phase such as FCC in the present case. The residue of the fit then shows the unindexed peaks more clearly and

it is easier to figure out which crystal structure is possible for the remaining peaks. This procedure was performed for all patterns. By doing this, it is found that the supplementary peaks could be associated with a C14 and a C15 phases.

The crystal parameters and abundance of each phase in all hydrogenated samples as determined by Rietveld's analysis are presented in Table 3.7.

**Table 3.7: Crystal parameters and abundance of each phase in hydrogenated:  $\text{Ti}_{1.1}\text{V}_{0.9}\text{Cr}_{1.1} + x \text{ wt } \% \text{ Zr}$  alloys for  $x=0, 2, 4, 8$  and  $12$ . Error on the last significant digit is indicated in parentheses**

Sample	Phase	Lattice parameter (Å)	Crystallite size (nm)	Phase abundance (%)
x=0	BCC	3.0375 (4)	20 (5)	93 (8)
	Ti	a=2.9622 (2)	11 (3)	7 (3)
		c=4.773 (6)		
x=2	FCC	4.2856 (6)	34 (3)	80 (2)
	C15	7.413 (1)	4 (2)	10 (2)
	C14	a=6.141 (7) c=7.262 (2)	6 (3)	10 (1)
x=4	BCC	3.1443 (1)	25 (5)	56 (4)
	FCC	4.2912 (2)	42 (2)	41 (4)
	C14	a=5.809 (2) c=8.03 (4)	11 (3)	3 (1)
x=8	FCC	4.2875(2)	16 (2)	72 (6)
	C15	7.605(7)	8 (3)	28 (3)
x=12	FCC	4.289 (2)	12 (2)	56 (6)
	C15	7.646 (4)	12 (1)	44 (6)

The lattice parameter of the BCC structure for the hydride of  $x=0$  is the same as the lattice parameter of the as-cast one. This confirms that the undoped sample wasn't hydrogenated at all. In the case of  $x = 2$ , the FCC phase abundance in the hydrogenated sample is less than the BCC abundance in the as-cast alloy (80% vs. 92%) while both C14 and C15 phases are more abundant in the hydrogenated sample.

For  $x = 4$ , there is a presence of both BCC and FCC phases in the hydrogenated alloy. This is surprising, considering that the hydrogen capacity is slightly higher than for  $x = 2$ .

It is well known that the monohydride of the BCC phase is a BCT (Body Centred Tetragonal) but, as the lattices parameters are very close to each other it is practically impossible to distinguish between the BCC and BCT phases.

However, the lattice parameter of the BCC phase in the hydrogenated state is much larger than in the as-cast state. From the difference in volume of the unit cells and assuming that, on average, a hydrogen atom occupies a volume of  $2.5 \text{ \AA}^3$ , we could estimate that the BCC phase in the hydrogenated state has a ratio of H/M of about 0.56 which is equivalent to 1 wt %.

When  $x = 8$ , we see that the hydrogenated alloy has 72 wt % of FCC phase which corresponds closely to the abundance of BCC phase in the as-cast alloy (68 wt %). Only the C15 phase is present in the hydrogenated sample and the abundance is almost the total of the C14 and C15 phases in the as-cast alloy. Thus, it seems that, upon hydrogenation, the C14 phase turns into a C15 phase.

Finally, for  $x = 12$ , the FCC phase has an abundance of 56 wt % which is lower than the abundance of the BCC phase in the as-cast alloy (66 wt %). As for  $x = 8$ , there is no C14 phase in the hydrogenated pattern.

For high addition of zirconium  $x > 8$ , the C14 phase was not detected by X-ray diffraction. This may be due to the fact that, upon hydrogenation, the crystallite size is reduced thus, broadening the peaks of this phase. As the C14 phase is already present in relatively small amount (less than 12 wt %) this makes that phase practically undetectable by X-ray diffraction as the peaks are merged into the background.

### **3.2.5 Air exposure effect**

For industrial production, it could be beneficial to be able to handle the cast alloys in air. This motivated us to investigate the air exposure effect on the alloy with 12 wt % of

zirconium. Figure 3.6 shows the activation curves for this alloy crushed in air, in argon and after two days of air exposure.

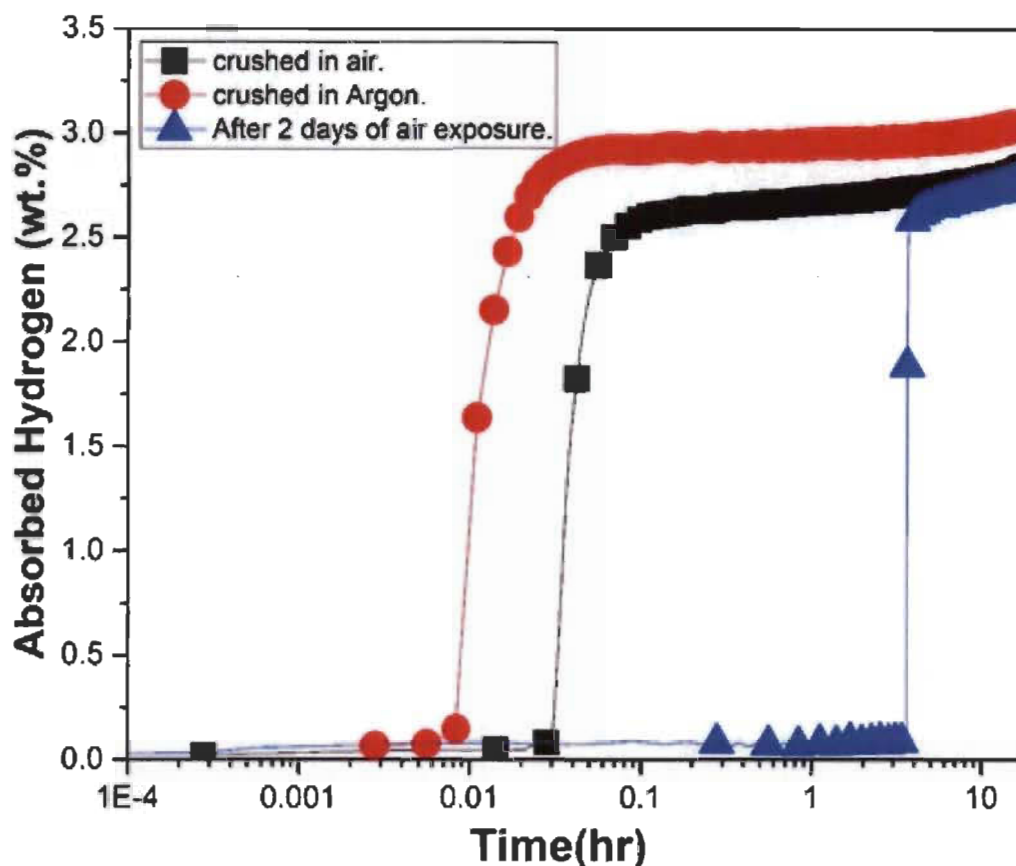


**Figure 3.6: First hydrogenation curves of  $\text{Ti}_1\text{V}_{0.9}\text{Cr}_{1.1} + 12 \text{ wt } \% \text{ Zr}$  crushed under argon and under air and after 2 days of air exposure at room temperature and under 2 MPa of hydrogen**

The sample crushed in air has a very short incubation time of 1.6 minutes while the sample after two days of air exposure presents a longer incubation time of 3.75 hours.

However, after incubation time the intrinsic kinetic is as fast for the sample exposed to the air two days as for the samples only crushed in air or in argon.

The longer incubation time shown by the sample stored in air for 2 days is most probably due to presence of surface oxide.

### 3.3 Conclusion

Addition of Zr generated a multiphase microstructure made of a main BCC phase and secondary phases. The secondary phase's abundance increased with Zr content. The two secondary phases were found to be Laves phases: a hexagonal C14 phase and a cubic C15 phase. The first hydrogenation kinetics of  $\text{Ti}_1\text{V}_{0.9}\text{Cr}_{1.1} + x \text{ wt } \% \text{ Zr}$  ( $x = 2, 4, 8, \text{ and } 12$ ) alloys was found to be increased with the amount of Zr.

Upon hydrogenation, most of the BCC phase transforms to the dihydride FCC phase but a small fraction of the BCC phase also seems to transform to a C15 phase with bigger lattice parameter, indicating that this phase also absorbs hydrogen.

For high zirconium loading ( $x > 8$ ), only the C15 phase is present in the hydride pattern beside the FCC phase. Therefore, hydrogenation seems to promote the transformation of C14 and some fraction of BCC phase into C15 phase.

The faster first hydrogenation of the alloys containing zirconium could be explained by the presence of the C14 and C15 secondary phases. This made the first hydrogenation at room temperature much faster.

Addition of 4 wt % of Zr produced fast kinetics and the highest hydrogen storage capacity while higher abundance of zirconium ( $x > 4$ ) leads to a decrease in hydrogen storage capacity.

The effect of air exposure was investigated for the sample doped with 12 wt % Zr. It was found that, for the first hydrogenation, air exposure produces a long incubation time and a slight decrease in the hydrogen capacity.



## Chapter 4: The article


### 4.1 Abstract

The effect of adding Zr on microstructure and hydrogen storage properties of BCC  $\text{Ti}_1\text{V}_{0.9}\text{Cr}_{1.1}$  synthesized by arc melting was studied. The microstructures of samples with Zr were multiphase with a main BCC phase and secondary Laves phases C15 and C14. The abundance of secondary phases increased with increasing amount of zirconium. We found that addition of Zr greatly enhanced the first hydrogenation kinetics. The addition of 4 wt % of Zr produced fast kinetics and high hydrogen storage capacity. Addition of higher amount of Zr had for effect of decreasing the hydrogen capacity. The reduction in hydrogen capacity might be due to the increased secondary phase abundance. The effect of air exposure was also studied. It was found that, for the sample with 12 wt % of Zr, exposure to the air resulted in appearance of an incubation time in the first hydrogenation and a slight reduction of hydrogen capacity.

Clicours.COM

## Article

# Microstructure and Hydrogen Storage Properties of $\text{Ti}_1\text{V}_{0.9}\text{Cr}_{1.1}$ Alloy with Addition of $x$ wt % Zr ( $x = 0, 2, 4, 8$ , and $12$ )

Salma Sleiman and Jacques Huot \* 

Hydrogen Research Institute, Université du Québec à Trois-Rivières, 3351 des Forges, Trois-Rivières, QC G9A 5H7, Canada; salma.sleiman@uqtr.ca

\* Correspondence: jacques.huot@uqtr.ca; Tel.: +1-819-376-5011 (ext. 3576); Fax: +1-819-376-5164

Received: 4 October 2017; Accepted: 28 November 2017; Published: 3 December 2017

**Abstract:** The effect of adding Zr on microstructure and hydrogen storage properties of BCC  $\text{Ti}_1\text{V}_{0.9}\text{Cr}_{1.1}$  synthesized by arc melting was studied. The microstructures of samples with Zr were multiphase with a main BCC phase and secondary Laves phases C15 and C14. The abundance of secondary phases increased with increasing amount of zirconium. We found that addition of Zr greatly enhanced the first hydrogenation kinetics. The addition of 4 wt % of Zr produced fast kinetics and high hydrogen storage capacity. Addition of higher amount of Zr had for effect of decreasing the hydrogen capacity. The reduction in hydrogen capacity might be due to the increased secondary phase abundance. The effect of air exposure was also studied. It was found that, for the sample with 12 wt % of Zr, exposure to the air resulted in appearance of an incubation time in the first hydrogenation and a slight reduction of hydrogen capacity.

**Keywords:** hydrogen storage; bcc alloys; kinetics; air exposure

## 1. Introduction

Hydrogen is considered a possible alternative energy carrier in the future. One of the most challenging barriers of using hydrogen is to establish a safe, reliable, compact, and cost-effective means of storing hydrogen [1–4]. Because of their high volumetric hydrogen capacity, metal hydrides could potentially replace the conventional storage in gaseous or liquid state. Moreover, metal hydrides are, in many respects, safe and cost effective [5,6]. Among the many different metal hydride systems, the Ti-based body-centred cubic (BCC) solid solution alloys are considered to be good candidates for hydrogen storage tanks because of their tunable pressure plateau and safety [7–10]. However, these alloys suffer from slow and difficult first hydrogenation, the so-called activation step [11]. Different approaches have been taken to overcome this drawback. These include heat treatment [12], addition of  $\text{Zr}_7\text{Ni}_{10}$  [12–16], or Zr [17,18] and by element substitution [19,20]. Another approach was made by Edalati K. et al. [21] who used high-pressure torsion to induce microstructural modification and so enhancing hydrogen storage properties of Ti–V BCC alloys. With respect to  $\text{Zr}_7\text{Ni}_{10}$  addition, the ease of activation may be due to the two-phase microstructure consisting of a main BCC phase and a secondary phase. Recently, Banerjee et al. [22] found that with increasing secondary phase concentration, faster kinetics was obtained but the hydrogen storage capacity was reduced. Moreover, Shashikala et al. [19] noticed that Zr is the element responsible for producing the secondary phase that ensures a rapid reaction with hydrogen and observed that hydrogen absorption capacity was decreased as the Zr content increased due to a greater fraction of Laves phase. In addition, Martinez and Santos found that  $\text{TiV}_{0.9}\text{Cr}_{1.1}$  alloy with addition of 4 wt % of  $\text{Zr}_7\text{Ni}_{10}$  showed fast hydrogenation kinetics and high capacity (3.6 wt %) [14]. Lately, Bellon et al. showed that by substituting Zr for V in the alloy  $\text{TiCrV}$  resulted in a two-phase structure made up of a main BCC structure and a less

abundant cubic-type Laves phase C15. They concluded that the Laves phase acts as a catalyst for the hydrogenation [17]. In this paper, we report our investigation on the effect of addition of Zr on the microstructure and hydrogen storage properties of  $\text{Ti}_1\text{V}_{0.9}\text{Cr}_{1.1}$ . Contrary to the work of Bellon et al., in the present investigation zirconium was not substituting for vanadium but instead added to the  $\text{TiV}_{0.9}\text{Cr}_{1.1}$  composition. By varying the Zr addition from 2 to 12 wt % we aimed to see how the amount of zirconium affect the relative abundance of BCC and Laves phases as well as their composition and the effect on hydrogen storage.

## 2. Results and Discussion

### 2.1. Microstructure Analysis

Figure 1 shows the backscattered electron micrographs of  $\text{Ti}_1\text{V}_{0.9}\text{Cr}_{1.1} + x$  wt % Zr alloys where  $x = 0, 2, 4, 8$ , and 12. It is clear that the microstructure changes with  $x$  content. Pure  $\text{Ti}_1\text{V}_{0.9}\text{Cr}_{1.1}$  (Figure 1a) shows a network of black areas structure. From EDX analysis these black areas were found to be titanium precipitates. Even with a slight doping of Zr ( $x = 2$ ), a bright secondary phase appeared. All the modified alloys were found to be multi-phase: a matrix phase and a bright phase. Dendrites appeared from  $x = 8$  and were clearly observed for  $x = 12$ . It is seen that more Zr leads to higher secondary phase abundance.

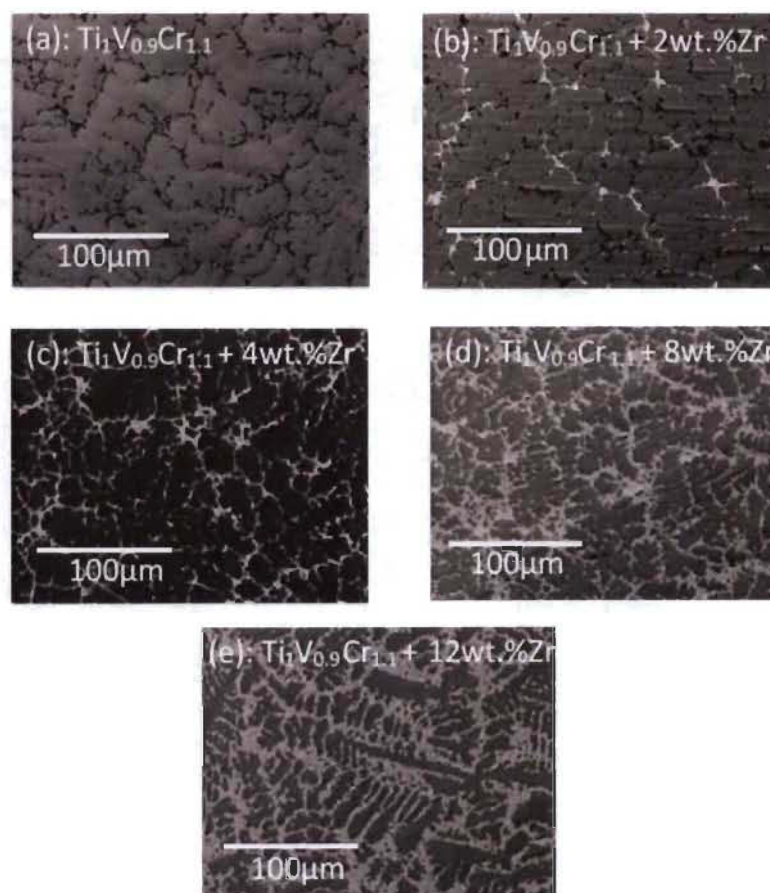


**Figure 1.** Backscattered electrons (BSE) micrographs of:  $\text{Ti}_1\text{V}_{0.9}\text{Cr}_{1.1} + x$  wt % Zr with  $x = 0$  (a); 2 (b); 4 (c); 8 (d); and 12 (e).

Using Image J software, the bright phase surface areas were measured. The percentage of the bright areas are 0, 4, 12, 26, and 35 respectively for  $x = 0, 2, 4, 8$ , and 12. It shows that, as the amount of doped Zr increases, the bright phase surface area is getting bigger. To determine the chemical composition, EDX measurement was performed on all alloys. Table 1 shows the bulk measured atomic abundance compared to the nominal composition for all alloys studied. We see that the bulk measured composition agrees with the nominal one in all cases. This was expected as all these elements have similar melting points.

**Table 1.** Bulk atomic abundance: nominal and as measured by EDX of:  $\text{Ti}_1\text{V}_{0.9}\text{Cr}_{1.1} + x \text{ wt } \% \text{ Zr}$  alloys for  $x = 0, 2, 4, 8$ , and 12. Error on the last significant digit is indicated in parentheses.

Sample		Ti (at %)	V (at %)	Cr (at %)	Zr (at %)
$x = 0$	Nominal composition	33	30	37	0
	Measurement	34.0(2)	29.8 (3)	36.2 (3)	0.0
$x = 2$	Nominal composition	32.6	29.7	36.6	1.1
	Measurement	32.8 (2)	29.4 (2)	36.4 (3)	1.4 (1)
$x = 4$	Nominal composition	32.3	29.3	36.2	2.2
	Measurement	34.0 (3)	28.2 (1)	35.2 (3)	2.6 (1)
$x = 8$	Nominal composition	31.6	28.7	35.4	4.3
	Measurement	32.3 (2)	27.7 (2)	34.5(3)	5.5 (1)
$x = 12$	Nominal composition	30.9	28.1	34.7	6.3
	Measurement	31.7 (2)	26.2 (2)	33.9 (2)	8.2 (1)

Using EDX, we also measured the atomic composition of each phase for all alloys. In Figure 2a representative of elemental mapping is shown for the compound  $\text{Ti}_1\text{V}_{0.9}\text{Cr}_{1.1} + 4 \text{ wt } \% \text{ Zr}$  alloy. Similar features were seen for the other alloys.

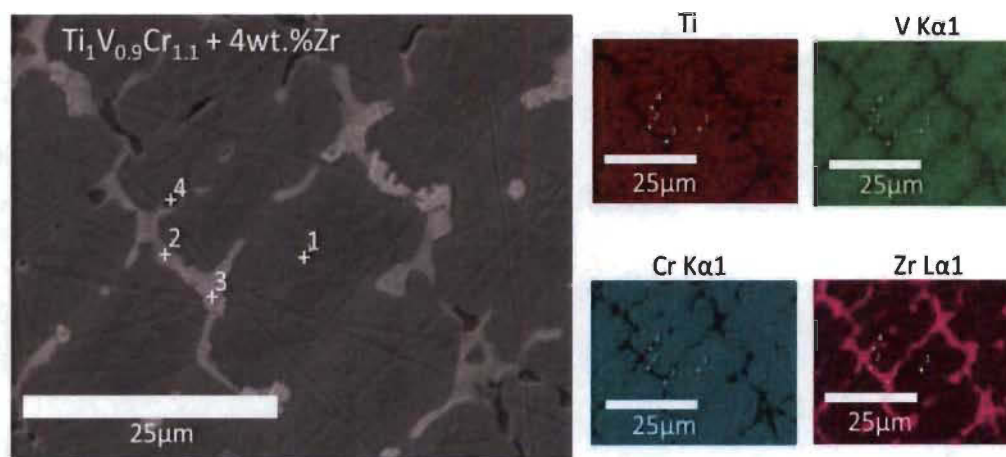


**Figure 2.** Backscattered electron micrograph of:  $\text{Ti}_1\text{V}_{0.9}\text{Cr}_{1.1} + 4 \text{ wt } \% \text{ Zr}$  alloy with elements mapping.

In these micrographs, specific locations are indicated by numbers. The matrix phase is numbered 1. Close inspection has shown that the bright secondary phase is in fact composed of two phases having different shades of white. Thus, two secondary phases were indexed. They are indicated by point 2 and point 3. Finally, the dark area is identified as point 4. The quantitative analysis at these specific locations are listed in the Tables 2–5. Table 2 presents the composition of the matrix (point 1) for all alloys.

**Table 2.** EDX analysis showing the elemental composition of the matrix (point 1) of:  $\text{Ti}_1\text{V}_{0.9}\text{Cr}_{1.1} + x$  wt % Zr alloys for  $x = 0, 2, 4, 8$ , and 12.

Sample	Ti (at %)	V (at %)	Cr (at %)	Zr (at %)
$x = 0$	27.8	33.8	38.4	0.0
$x = 2$	27.4	33.4	38.9	0.3
$x = 4$	25.8	35.0	38.9	0.3
$x = 8$	29.3	31.6	38.2	0.9
$x = 12$	28.5	31.7	38.9	0.9

From Table 2, we see that the matrix is a Ti–V–Cr solid solution with inclusion of only a very small amount of Zr (<1 at %). The matrix composition does not significantly change when more zirconium is added. On average, the atomic composition of the matrix is  $\text{Ti}_{0.84}\text{V}_1\text{Cr}_{1.2}\text{Zr}_{0.03}$  which is quite different than the nominal value. The main difference is that, compared to the nominal composition, the titanium proportion is reduced, the vanadium amount increased, and the chromium abundance stays almost the same. The zirconium abundance in the matrix is always less than 1 at % which is far from the nominal composition. As the amount of zirconium was very small in the matrix, we expect that zirconium will be mainly confined in the secondary phases. This could be seen in Tables 3 and 4 which show the atomic composition of the two secondary phases. Secondary phase one (point 2) is rich in Ti and Zr while secondary phase two (point 3) has a relatively high content of the four elements.

**Table 3.** EDX analysis showing the elemental composition of the secondary phase 1 (point 2) of  $\text{Ti}_1\text{V}_{0.9}\text{Cr}_{1.1} + x$  wt % Zr alloys for  $x = 0, 2, 4, 8$ , and 12.

Sample	Ti (at %)	V (at %)	Cr (at %)	Zr (at %)
$x = 2$	64.0	7.0	6.2	22.8
$x = 4$	64.0	6.7	6.2	23.1
$x = 8$	58.3	6.8	4.6	30.3
$x = 12$	55.8	7.2	5.1	32.0

From Table 3, we see that the secondary phase 1 (point 2) is close to composition  $\text{Ti}_{1.9}\text{V}_{0.2}\text{Cr}_{0.2}\text{Zr}_{0.7}$  for  $x = 2$  or 4 and to composition  $\text{Ti}_{1.7}\text{V}_{0.2}\text{Cr}_{0.2}\text{Zr}_{0.9}$  for  $x = 8$  and 12. To our knowledge, there are no quaternary alloys that have stoichiometry close to these. Therefore, this secondary phase may be metastable. It has to be mentioned that, when  $x$  is higher than 8 there is a higher proportion of zirconium and lower proportion of titanium while the abundances of the two other elements are constant.

Table 4 shows the composition of secondary phase 2 (point 3). This phase has an almost constant composition  $\text{Ti}_{1.0}\text{V}_{0.4}\text{Cr}_{1.1}\text{Zr}_{0.5}$  and also has a high zirconium content but here chromium is the most abundant element. Contrary to secondary phase 1, the relative atomic abundance of this phase does not vary with increasing of  $x$ .

**Table 4.** EDX analysis showing the elemental composition of secondary phase 2 (point 3) of:  $\text{Ti}_1\text{V}_{0.9}\text{Cr}_{1.1} + x$  wt % Zr alloys for  $x = 0, 2, 4, 8$ , and 12.

Sample	Ti (at %)	V (at %)	Cr (at %)	Zr (at %)
$x = 2$	33.7	12.3	38.0	16.0
$x = 4$	32.8	12.3	37.9	17.0
$x = 8$	32.8	15.5	33.6	18.1
$x = 12$	28.5	14.8	36.5	20.2

Close inspection of Figure 2 also indicates that secondary phase 2 is usually on the edge of the bright surfaces while secondary phase 1 is more in the centre of the bright areas. Thus, it seems that



secondary phase 2 is bridging secondary phase 1 with the matrix. Close inspection of Tables 3 and 4 demonstrates that the chemical composition of the secondary phases slightly changes when  $x$  increases. The main characteristics of these phases are however constant. When  $x$  increases, secondary phase 1 remains rich in titanium and zirconium with the proportion of titanium slightly decreasing and zirconium increasing. Regarding secondary phase 2, this phase is rich in chromium but also the proportions of zirconium and titanium relatively important. When  $x$  increase zirconium content increases, titanium abundance decreases and chromium only slightly decreases. Chemical composition of the black phase (point 4) was measured and the results are reported in Table 5.

**Table 5.** EDX analysis showing the elemental composition at point 4 of:  $\text{Ti}_{1.9}\text{V}_{0.9}\text{Cr}_{1.1} + x \text{ wt \% Zr}$  alloys for  $x = 0, 2$ , and 4.

Sample	Ti (at %)	V (at %)	Cr (at %)	Zr (at %)
$x = 0$	87.7	7.0	5.3	0.0
$x = 2$	88.2	3.3	2.0	6.5
$x = 4$	79.6	6.8	5.6	8.0

It is evident that the black areas are titanium precipitates. The amount of precipitation tends to decrease with increasing Zr content and for 8 and 12 wt % of Zr there are no Ti-precipitates.

## 2.2. Structural Characterization

Figure 3 shows the XRD pattern of all the studied samples in the as-cast state. The major diffraction peaks of all as cast alloys can be identified as BCC phase (space group  $Im\bar{3}m$ ). Small peaks appeared as the zirconium doping increases. These peaks are surely related to the secondary phases. Due to the smallness of the peaks and their relatively small numbers, indexing them is not obvious. However, as demonstrated by Akiba and Iba, Laves phases could be closely related to BCC alloys [7]. Laves phases are well known intermetallic phases that crystallize in three different structures: a cubic  $\text{MgCu}_2$ -type (Space group  $Fd\bar{3}m$ ), a hexagonal  $\text{MgZn}_2$ -type (space group  $P6_3/mmc$ ), or a hexagonal  $\text{MgNi}_2$ -type (Space group  $P6_3/mmc$ ). Following the *Strukturbericht* nomenclature, these phases will be thereafter respectively designated C15, C14, and C36. In the specific case of Ti–V–Cr BCC alloys, it was also shown by Bellon et al. [17] that when zirconium is substituted for vanadium in these alloys there is the appearance of a C15 Laves phase.

We analyzed our diffraction patterns by Rietveld's refinement. The obtained crystal parameters and the abundance of each phase in all samples are shown in Table 6. In these refinements, we tried to index the secondary phases' peaks with Laves phases. We found that the peaks could be indexed by using two Laves phases, namely the C15 and C14 phases. Tentatively, the C14 phase was assigned to the composition  $\text{Ti}_{1.9}\text{V}_{0.2}\text{Cr}_{0.2}\text{Zr}_{0.7}$  (secondary phase 1) and the C15 phase to the composition  $\text{Ti}_{1.0}\text{V}_{0.4}\text{Cr}_{1.1}\text{Zr}_{0.5}$  (secondary phase 2). However, as it is difficult to distinguish between Ti, V, and Cr by X-ray diffraction the exact assignment could be only done by using neutron diffraction. Also, the problem with these compositions is that the ratio A/B is not 2 as it should be. For these reasons, we should stress that the indexing of C14 and C15 is tentative and more experiments are needed in order to have the definitive crystal structure of the secondary phases. We are now undertaking neutron experiments and these will be reported in a future paper. In the present case, we could conclude that using two Laves phases for fitting the secondary phase peaks confirm the finding of electron microscopy where two different secondary phases were found. We should also point out that, on Figure 3 only the main peaks of C14 and C15 have been indexed. As these two phases have small abundances, only the main peaks are showing in the diffraction patterns and indexing all possible peaks will have confused the reader, especially for overlapping peaks that are so small that they are undistinguishable from the background. Referring to Table 6 at which the phase abundances are presented for all studied alloys, we see that the total abundance of C15 + C14 phases roughly matches the abundance measured from image J.

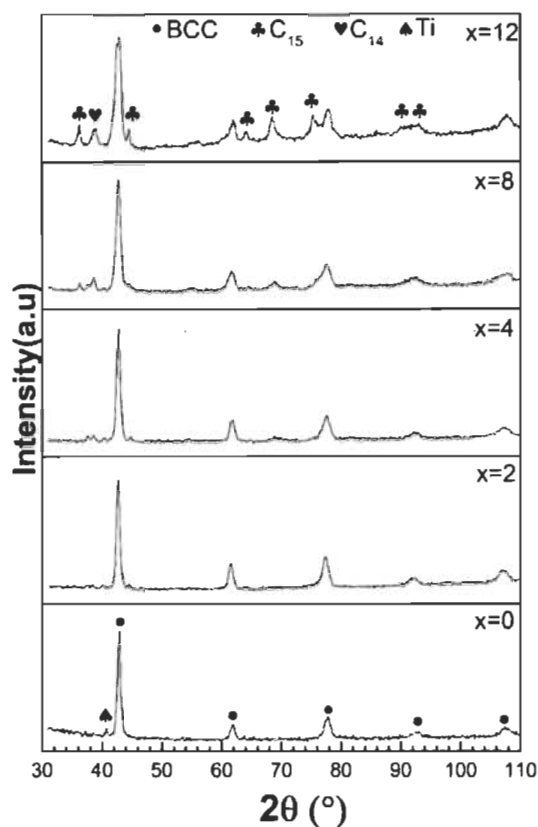


Figure 3. X-ray diffraction patterns of as cast:  $\text{Ti}_1\text{V}_{0.9}\text{Cr}_{1.1} + x$  wt % Zr alloys with  $x = 0, 2, 4, 8$ , and  $12$ .

Table 6. Crystal parameters and abundance of each phase in as cast:  $\text{Ti}_1\text{V}_{0.9}\text{Cr}_{1.1} + x$  wt % Zr alloys for  $x = 0, 2, 4, 8$ , and  $12$ . Error on the last significant digit is indicated in parentheses.

Sample	Phase	Lattice Parameter (Å)	Crystallite Size (nm)	Phase Abundance (%)	Bright Area Abundance (%)
$x = 0$	BCC	3.0379 (9)	24 (2)	97 (3)	0
	Ti	$a = 2.961$ (4)	13 (2)	3 (3)	
		$c = 4.773$ (1)			
$x = 2$	BCC	3.0479 (5)	22 (1)	92 (2)	4
	C15	7.172 (7)	14 (7)	2 (1)	
	C14	$a = 5.903$ (9)	8 (2)	6 (2)	
$x = 4$	BCC	3.0470 (7)	23 (2)	89 (3)	12
	C15	7.153 (5)	20 (8)	3 (1)	
	C14	$a = 5.935$ (1)	5 (1)	8 (3)	
$x = 8$	BCC	3.0452 (1)	38 (9)	68 (5)	26
	C15	7.180 (5)	6 (1)	21 (4)	
	C14	$a = 5.849$ (7)	6 (1)	11 (2)	
$x = 12$	BCC	3.0310 (1)	8 (3)	66 (4)	35
	C15	6.099 (7)	10 (1)	22 (2)	
	C14	$a = 5.815$ (2)	3 (1)	12 (2)	
		$c = 8.01$ (1)			



### 2.3. Activation Process

The first hydrogenation (activation) of as-cast  $\text{Ti}_1\text{V}_{0.9}\text{Cr}_{1.1} + x \text{ wt } \% \text{ Zr}$  alloys was performed at room temperature under a hydrogen pressure 2MPa after the alloys were crushed in argon. Results are presented in Figure 4. The first hydrogenation for  $x = 0$  is practically impossible. This sample did not absorb hydrogen even after 900 min of hydrogen exposure. Adding only 2 wt % of Zr to the alloy resulted in a good hydrogen uptake, but the full hydrogenation still takes about 10 h. Increasing  $x$  value to 4 wt % had the effect of greatly enhancing the kinetics and full hydrogenation was achieved after 150 min. Further increase of zirconium content slightly improved the kinetics but the total capacity decreased. Among all doped samples, the one with 12 wt % Zr has the fastest activation kinetics, reaching maximum capacity within 3 min. For hydrogen storage purposes, the optimum amount of zirconium seems to be 4 wt %. However, even if the capacity slightly decreases with addition of more zirconium, the fact is that even when the amount of secondary phases is high, the decrease in capacity is not very important. For example, in the alloy with 12 wt % of Zr the secondary phases comprise between 35 wt % (as measured from SEM images) and 34 wt % (as determined from Rietveld refinement). Taking the low estimation of 34 wt %, if these secondary phases do not absorb hydrogen, and assuming that pure BCC absorbs about 4 wt % of hydrogen, we should expect a capacity of about 2.7 wt % which is clearly not the case. The measured capacity could not be explained by the presence of the BCC alloy itself. Thus, we have evidence that, at least one of the secondary phases absorbs hydrogen. Nonetheless, this then raises the question of the kinetic curves. Except for the 2 wt % Zr alloy, all activation curves do not show any kinks or slope change. This is the signature of a single-phase alloy which is evidently not the case here. However, it has been shown by Akiba and Iba [7] that the BCC Laves phase related alloys could actually be formed by a BCC phase and a Laves phase and still display a single phase behaviour upon hydrogen absorption. It seems to be the case in the present system.

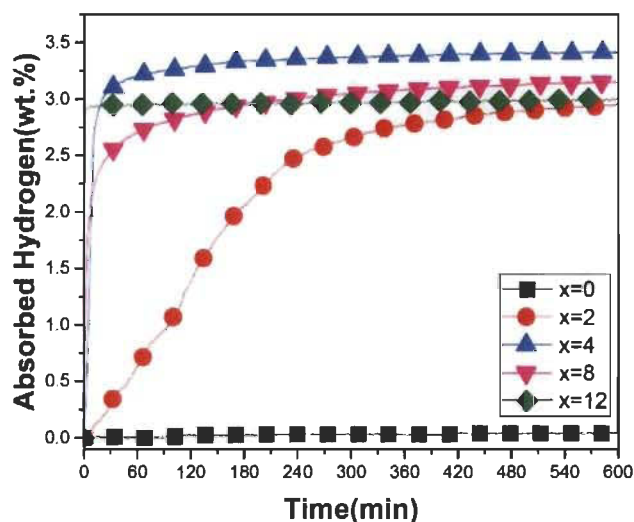


**Figure 4.** Activation curves of:  $\text{Ti}_1\text{V}_{0.9}\text{Cr}_{1.1} + x \text{ wt } \% \text{ Zr}$  for  $x = 0, 2, 4, 8$ , and 12 at room temperature under 2MPa of hydrogen.

Interphase boundaries probably play a role in the activation. Similar investigation in other systems seems to point that way. Nanocrystallinity is also well known to enhance hydrogenation/dehydrogenation kinetics [6]. However, in the present case it is not the main factor as evidenced by Table 6. From this table, we see that the samples with  $x = 2$  and  $x = 4$  have almost the same crystallite size but their activation curve is drastically different. Moreover, the sample with  $x = 8$  has a larger crystallite size but the hydrogenation is faster. Therefore, nanocrystallinity alone

could not explain the behaviour of this system. Dislocations and defects could lead to a faster first hydrogenation in metal hydrides and was shown for cold rolled alloys [23,24].

Another explanation for the quick activation of alloys with zirconium addition may be stability of the FCC hydride. As the matrix of the Zr-containing alloys has a stoichiometry different than the nominal value and also, taking into account the fact that the BCC alloy contains some zirconium, it may well result in some change of the formation enthalpy of the FCC hydride phase. A more stable hydride may result in an easier activation but to have a definitive answer, the pressure-composition isotherms have to be registered. Such an investigation is planned for the near future.

#### 2.4. XRD Patterns after Hydrogenation

In this set of experiments, in order to study the crystal structure of the hydride phase, the absorption experiment was stopped after reaching full hydrogenation and thereafter the pressure just lowered to one bar of hydrogen. No vacuum was applied to the sample to be sure that no desorption occurred during removal of the sample holder. In separated tests, we exposed the samples to a pressure of 10 kPa and no desorption was noticed.

Figure 5 shows X-ray diffraction patterns of all alloys after first exposure to hydrogen. We see that for  $x = 0$ , the structure is still BCC which confirms what was seen on Figure 4. For  $x = 2$ , the crystal structure is essentially FCC which is usually the crystal structure adopted by a fully hydrided BCC alloy. The FCC phase is also seen in the patterns for  $x = 4, 8$ , and  $12$  but there are clearly other phases present. Indexation of the supplementary peaks is helped by doing a Rietveld refinement. Even if, in a Rietveld refinement prior knowledge of the phase present is mandatory, we could use this technique to first fit the patterns by using the known phase such as FCC in the present case. The residue of the fit then shows the unindexed peaks more clearly and it is easier to figure out which crystal structure is possible for the remaining peaks. This is the procedure we performed for all patterns and by doing it we found that the supplementary peaks could be associated with a C14 and a C15 phases.

The crystal parameters and abundance of each phase in all hydrogenated samples as determined by Rietveld's analysis are presented in Table 7. For  $x = 0$ , the sample did not absorb hydrogen and the crystal structure is still BCC. There is practically no change in the lattice parameter and crystallite size, which means that there was no reaction with hydrogen. In the case of  $x = 2$ , the FCC phase abundance in the hydrogenated sample is less than the BCC abundance in the as-cast alloy (80% vs. 92%) while both C14 and C15 phases are more abundant in the hydrogenated sample. The reason for this behaviour is unclear but a premature conclusion should be avoided because the abundance values are associated with relatively high experimental errors. For  $x = 4$ , there is a presence of both BCC and FCC phases in the hydrogenated alloy. This is surprising, considering that the hydrogen capacity is slightly higher than for  $x = 2$ . It is well known that the monohydride of the BCC phase is a BCT (Body Centred Tetragonal) but, as the lattices parameters are very close to each other it is practically impossible to distinguish between the BCC and BCT phases. However, the lattice parameter of the BCC phase in the hydrogenated state is much bigger than in the as-cast state. From the difference in volume of the unit cells and assuming that, on average, a hydrogen atom occupies a volume of  $2.5 \text{ \AA}^3$ , we could estimate that the BCC phase in the hydrogenated state has a ratio of H/M of about 0.56. When  $x = 8$ , we see that the hydrogenated alloy has 72 wt % of FCC phase which corresponds closely to the abundance of BCC phase in the as-cast alloy (68 wt %). Only the C15 phase is present in the hydrogenated sample and the abundance is almost the total of the C14 and C15 phases in the as-cast alloy. Thus, it seems that, upon hydrogenation, the C14 phase turns into a C15 phase. Finally, for  $x = 12$ , the FCC phase has an abundance of 56 wt % which is lower than the abundance of the BCC phase in the as-cast alloy (66 wt %). As for  $x = 8$ , there is no C14 phase in the hydrogenated pattern.

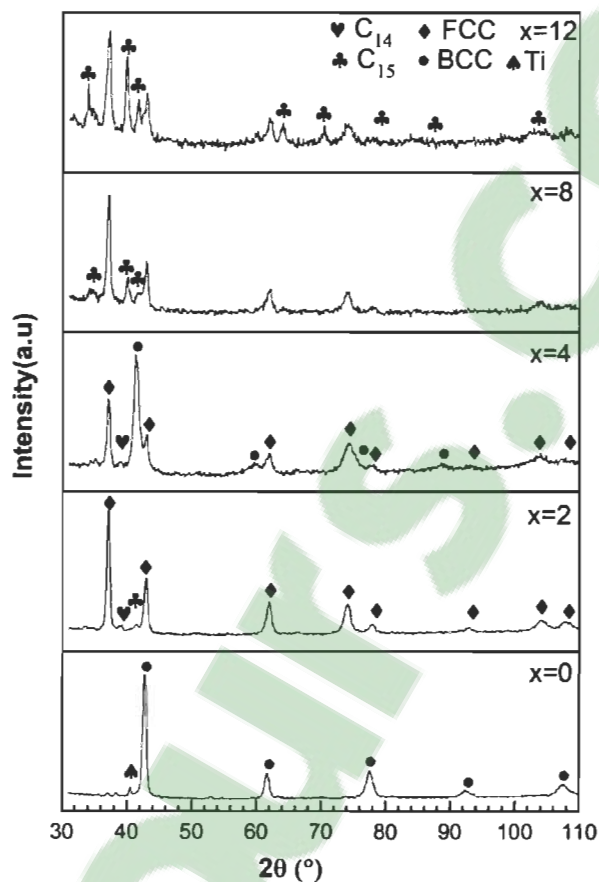


**Figure 5.** X-ray diffraction patterns of:  $\text{Ti}_1\text{V}_{0.9}\text{Cr}_{1.1} + x$  wt % Zr alloys in the hydrogenated state for  $x = 0, 2, 4, 8$ , and  $12$ .

**Table 7.** Crystal parameters and abundance of each phase in hydrogenated:  $\text{Ti}_1\text{V}_{0.9}\text{Cr}_{1.1} + x$  wt % Zr alloys for  $x = 0, 2, 4, 8$ , and  $12$ . Error on the last significant digit is indicated in parentheses.

Sample	Phase	Lattice Parameter (Å)	Crystallite Size (nm)	Phase Abundance (%)
$x = 0$	BCC	3.0375 (4)	20 (5)	93 (8)
	Ti	$a = 2.9622$ (2) $c = 4.773$ (6)	11 (3)	7 (3)
$x = 2$	FCC	4.2856 (6)	34 (3)	80 (2)
	C15	7.413 (1)	4 (2)	10 (2)
	C14	$a = 6.141$ (7)	6 (3)	10 (1)
		$c = 7.262$ (2)		
$x = 4$	BCC	3.1443 (1)	25 (5)	56 (4)
	FCC	4.2912 (2)	42 (2)	41 (4)
	C14	$a = 5.809$ (2)	11 (3)	3 (1)
		$c = 8.03$ (4)		
$x = 8$	FCC	4.2875(2)	16 (2)	72 (6)
	C15	7.605(7)	8 (3)	28 (3)
$x = 12$	FCC	4.289 (2)	12 (2)	56 (6)
	C15	7.646 (4)	12 (1)	44 (6)

For high addition of zirconium  $x > 8$ , the C14 phase was not detected by X-ray diffraction. This may be due to the fact that, upon hydrogenation, the crystallite size is reduced thus, broadening the peaks of this phase. As C14 phase is already present in relatively small amount (less than 12 wt %) this makes that phase practically undetectable by X-ray diffraction as the peaks are merged into the background.

### 2.5. Air Exposure Effect

For industrial production, it could be beneficial to be able to handle the cast alloys in air. This motivated us to investigate the air resistance of the alloy with 12 wt % of zirconium. Figure 6 shows the activation curves for this alloy crushed in air, in argon and after two days of air exposure. The sample crushed in air has a very short incubation time of 1.76 min while the sample after two days of air exposure presents a longer incubation time of 3.75 h. However, after incubation time the intrinsic kinetic is as fast for the sample exposed to the air two days as for the samples only crushed in air or in argon. The longer incubation time shown by the sample stored in air for two days is most probably due to the presence of surface oxide.

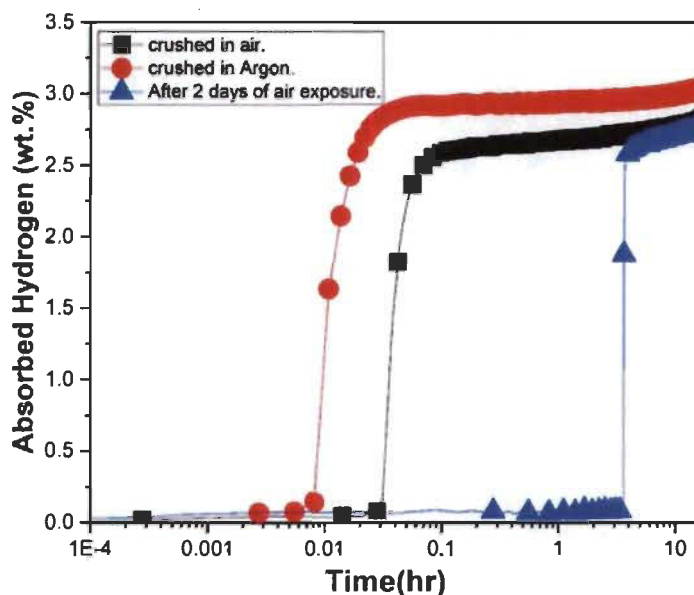


**Figure 6.** First hydrogenation curves of  $\text{Ti}_1\text{V}_{0.9}\text{Cr}_{1.1}$  + 12 wt % Zr crushed under argon and under air and after two days of air exposure at room temperature and under 2MPa of hydrogen.

### 3. Materials and Methods

Synthesis of  $\text{Ti}_1\text{V}_{0.9}\text{Cr}_{1.1} + x$  wt % Zr alloys were performed using an arc melting apparatus. The raw materials were purchased from Alfa-Aesar (Ward Hill, MA, USA) and had the following purity: Ti sponge (99.95%), V pieces (99%), Cr pieces (99%), and Zr sponge (99.95%). They were mixed at the desired stoichiometry and melted together under argon atmosphere. To ensure homogeneity, each pellet was melted, turned over, and remelted three times. Each pellet was then hand crushed using a steel mortar and pestle under argon atmosphere. Crushing in air was performed only for the air exposed sample. The material was filled into a sample holder and kept under vacuum for one hour at room temperature before exposing it to hydrogen. The hydrogen sorption properties were measured using a homemade Sievert's type apparatus. The measurements were done at room temperature under a hydrogen pressure of 20 MPa for absorption. The crystal structure was determined by X-ray

powder diffraction on a Bruker D8 focus apparatus with Cu K $\alpha$  radiation (Bruker AXS INC, Madison, WI, USA). Lattice parameters were evaluated by Rietveld's refinement of the X-ray patterns using Topas software [25]. Microstructure and chemical analysis were performed using a JEOL-JSM 5500 scanning electron microscopy (Ebay, Carson, CA, USA) equipped with an EDX (energy dispersive X-ray) apparatus from Oxford Instruments. The percentage of different phases was analyzed by image J software [26,27].

#### 4. Conclusions

The first hydrogenation kinetics of Ti<sub>1</sub>V<sub>0.9</sub>Cr<sub>1.1</sub> + *x* wt % Zr (*x* = 2, 4, 8, and 12) alloys was found to be increased with the amount of Zr. Doping with Zr generated a multiphase microstructure made of a main BCC phase and secondary phases. The secondary phases abundance increased with Zr content. The two secondary phases were found to be Laves phases: a hexagonal C14 phase and a cubic C15 phase. Upon hydrogenation, most of the BCC phase transforms to the dihydride FCC phase but a small fraction of the BCC phase also seems to transform to a C15 phase with bigger lattice parameter, indicating that this phase also absorbed hydrogen. For high zirconium loading (*x* > 8), only C15 phase is present in the hydride pattern beside the FCC phase. Therefore, hydrogenation seems to promote the transformation of C14 and some fraction of BCC phase into C15 phase. The faster first hydrogenation of the alloys containing zirconium could be explained by the presence of the C14 and C15 secondary phases. This made the first hydrogenation at room temperature much faster. Addition of 4 wt % of Zr produced fast kinetics and the highest hydrogen storage capacity while higher abundance of zirconium (*x* > 4) leads to decrease in hydrogen storage capacity. We also found that air exposure has a relatively small impact on the activation of Ti<sub>1</sub>V<sub>0.9</sub>Cr<sub>1.1</sub> + 12 wt % Zr alloy.

**Acknowledgments:** This investigation was supported by a NSERC (Natural Sciences and Engineering Research Council of Canada) discovery grant which also covered the cost of publishing in open access. We would like to thank A. Lejeune for electron microscopy experiments.

**Author Contributions:** All experiments, except electron microscopy, were performed by Salma Sleiman under the supervision of Jacques Huot.

**Conflicts of Interest:** The authors declare no conflict of interest.

#### References

1. Jena, P. Materials for hydrogen storage: Past, present, and future. *J. Phys. Chem. Lett.* **2011**, *2*, 206–211. [[CrossRef](#)]
2. Schlapbach, L.; Züttel, A. Hydrogen-storage materials for mobile applications. *Nature* **2001**, *414*, 353–358. [[CrossRef](#)] [[PubMed](#)]
3. Züttel, A. Materials for hydrogen storage. *Mater. Today* **2003**, *6*, 24–33. [[CrossRef](#)]
4. Züttel, A. Hydrogen storage and distribution systems. *Mitig. Adapt. Strateg. Glob. Chang.* **2007**, *12*, 343–365. [[CrossRef](#)]
5. Gambini, M.; Manno, M.; Vellini, M. Numerical analysis and performance assessment of metal hydride-based hydrogen storage systems. *Int. J. Hydrog. Energy* **2008**, *33*, 6178–6187. [[CrossRef](#)]
6. Sakintuna, B.; Lamari-Darkrim, F.; Hirscher, M. Metal hydride materials for solid hydrogen storage: A review. *Int. J. Hydrog. Energy* **2007**, *32*, 1121–1140. [[CrossRef](#)]
7. Akiba, E.; Iba, H. Hydrogen absorption by laves phase related BCC solid solution. *Intermetallics* **1998**, *6*, 461–470. [[CrossRef](#)]
8. Kuriwa, T.; Tamura, T.; Amemiya, T.; Fuda, T.; Kamegawa, A.; Takamura, H.; Okada, M. New V-based alloys with high protium absorption and desorption capacity. *J. Alloys Compd.* **1999**, *293*, 433–436. [[CrossRef](#)]
9. Okada, M.; Kuriwa, T.; Tamura, T.; Takamura, H.; Kamegawa, A. Ti–V–Cr BCC Alloys with high protium content. *J. Alloys Compd.* **2002**, *330*, 511–516. [[CrossRef](#)]
10. Tamura, T.; Kazumi, T.; Kamegawa, A.; Takamura, H.; Okada, M. Protium absorption properties and protide formations of Ti–Cr–V alloys. *J. Alloys Compd.* **2003**, *356*, 505–509. [[CrossRef](#)]



11. Itoh, H.; Arashima, H.; Kubo, K.; Kabutomori, T. The influence of microstructure on hydrogen absorption properties of Ti–Cr–V alloys. *J. Alloys Compd.* **2002**, *330*, 287–291. [\[CrossRef\]](#)
12. Fruchart, D.; De Rango, P.; Charbonnier, J.; Miraglia, S.; Rivoirard, S.; Skryabina, N.; Jehan, M. Nanocrystalline Composite for Storage of Hydrogen. U.S. Patent No. 8,012,452, 6 September 2011.
13. Bibienne, T.; Bobet, J.-L.; Huot, J. Crystal structure and hydrogen storage properties of body centered cubic 52Ti–12V–36Cr alloy doped with Zr<sub>7</sub>Ni<sub>10</sub>. *J. Alloys Compd.* **2014**, *607*, 251–257. [\[CrossRef\]](#)
14. Martínez, A.; dos Santos, D.S. Hydrogen absorption/desorption properties in the TiCrV based alloys. *Mater. Res.* **2012**, *15*, 809–812. [\[CrossRef\]](#)
15. Miraglia, S.; de Rango, P.; Rivoirard, S.; Fruchart, D.; Charbonnier, J.; Skryabina, N. Hydrogen sorption properties of compounds based on BCC Ti<sub>1–x</sub>V<sub>1–y</sub>Cr<sub>1+x+y</sub> alloys. *J. Alloys Compd.* **2012**, *536*, 1–6. [\[CrossRef\]](#)
16. Skryabina, N.; Fruchart, D.; Medvedeva, N.A.; de Rango, P.; Mironova, A.A. Correlation between the hydrogen absorption properties and the vanadium concentration of Ti–V–Cr based alloys. *Solid State Phenom.* **2017**, *257*, 165–172. [\[CrossRef\]](#)
17. Bellon, D.; Martinez, A.; Barreneche, D.; dos Santos, D. A structural study of the hydrogen absorption properties by replacing vanadium with zirconium in metal alloys. *J. Phys. Conf. Ser.* **2016**, *687*, 012057. [\[CrossRef\]](#)
18. Kamble, A.; Sharma, P.; Huot, J. Effect of doping and particle size on hydrogen absorption properties of BCC solid solution 52Ti–12V–36Cr. *Int. J. Hydrog. Energy* **2017**, *42*, 11523–11527. [\[CrossRef\]](#)
19. Shashikala, K.; Banerjee, S.; Kumar, A.; Pai, M.; Pillai, C. Improvement of hydrogen storage properties of TiCrV alloy by Zr substitution for Ti. *Int. J. Hydrog. Energy* **2009**, *34*, 6684–6689. [\[CrossRef\]](#)
20. Yoo, J.-H.; Shim, G.; Yoon, J.-S.; Cho, S.-W. Effects of substituting Al for Cr in the Ti<sub>0.32</sub>Cr<sub>0.43</sub>V<sub>0.25</sub> alloy on its microstructure and hydrogen storage properties. *Int. J. Hydrog. Energy* **2009**, *34*, 1463–1467. [\[CrossRef\]](#)
21. Edalati, K.; Shao, H.; Emami, H.; Iwaoka, H.; Akiba, E.; Horita, Z. Activation of titanium–vanadium alloy for hydrogen storage by introduction of nanograins and edge dislocations using high-pressure torsion. *Int. J. Hydrog. Energy* **2016**, *41*, 8917–8924. [\[CrossRef\]](#)
22. Banerjee, S.; Kumar, A.; Ruz, P.; Sengupta, P. Influence of laves phase on microstructure and hydrogen storage properties of Ti–Cr–V based alloy. *Int. J. Hydrog. Energy* **2016**, *41*, 18130–18140. [\[CrossRef\]](#)
23. Huot, J.; Tournant, M. Hydrogen sorption enhancement in cold-rolled and ball-milled CaNi<sub>5</sub>. *J. Mater. Sci.* **2017**, *52*, 11911–11918. [\[CrossRef\]](#)
24. Tournant, M.; Huot, J. Hydrogen sorption enhancement in cold rolled LaNi<sub>5</sub>. *J. Alloys Compd.* **2014**, *595*, 22–27. [\[CrossRef\]](#)
25. Bruker, A.X.S. TOPAS V3: General profile and structure analysis software for powder diffraction data. In *User's Manual*; Bruker AXS: Karlsruhe, Germany, 2005.
26. Abramoff, M.D.; Magalhaes, P.J.; Ram, S.J. Image processing with imageJ. *Biophotonics Int.* **2004**, *11*, 36–42.
27. Collins, T.J. ImageJ for microscopy. *Biotechniques* **2007**, *43*, 25–30. [\[CrossRef\]](#) [\[PubMed\]](#)



© 2017 by the authors. Licensee MDPI, Basel, Switzerland. This article is an open access article distributed under the terms and conditions of the Creative Commons Attribution (CC BY) license (<http://creativecommons.org/licenses/by/4.0/>).

## Conclusions and perspectives

In this master's thesis the effect of Zr addition to TiVCr alloy was studied. The microstructure, crystal structure and hydrogen storage properties were investigated.

We found that without addition of Zr, the activation was practically impossible. Adding Zr even with a small percentage by weight (2 wt %) the activation became possible. This is attributed to change in the microstructure and to appearance of secondary phases. These secondary phases ensure a rapid reaction with hydrogen.

By this work, it is clearly shown that addition of Zr is an effective way for enhancing the activation of  $\text{Ti}_1\text{V}_{0.9}\text{Cr}_{1.1}$  BCC alloy without any prior treatment. Moreover,  $\text{Ti}_1\text{V}_{0.9}\text{Cr}_{1.1} + 4 \text{ wt } \% \text{ Zr}$  can be a good candidate for hydrogen storage having fast kinetics and high storage capacity. In addition, we found that we are able to handle  $\text{Ti}_1\text{V}_{0.9}\text{Cr}_{1.1} + 12 \text{ wt } \% \text{ Zr}$  alloy in air and this give a benefit for large-scale production.

During this work, X-ray diffraction did not allow to identify the exact chemical compositions of secondary phases since the distinction between Ti, V and Cr is difficult by that technique, so it would be interesting to investigate the chemical compositions of C14 and C15 phases by neutron diffraction. As a future work, the pressure-composition isotherms should be conducted to assess the influence of Zr on the thermodynamic parameters as well as the stability of the hydride phase.

Regarding the production cost of alloys for hydrogen storage and since the 4wt% addition of Zr is the optimum case, we think that replacing vanadium by niobium in TiVCr + 4 wt % Zr could be promising. The reason is that the cost of niobium is about six times lower than vanadium, so such a substitution could be taken into consideration.



## REFERENCES

- [1] B. Johnston, M. C. Mayo, and A. Khare, "Hydrogen: the energy source for the 21st century," *Technovation*, vol. 25, no. 6, pp. 569-585, 2005.
- [2] N. A. Kelly, T. L. Gibson, M. Cai, J. A. Spearot, and D. B. Ouwerkerk, "Development of a renewable hydrogen economy: optimization of existing technologies," *International Journal of Hydrogen Energy*, vol. 35, no. 3, pp. 892-899, 2010.
- [3] I. Dincer and A. S. Joshi, "Hydrogen production methods," in *Solar Based Hydrogen Production Systems*: Springer, 2013, pp. 7-20.
- [4] A. Züttel, A. Remhof, A. Borgschulte, and O. Friedrichs, "Hydrogen: the future energy carrier," *Philosophical Transactions of the Royal Society of London A: Mathematical, Physical and Engineering Sciences*, vol. 368, no. 1923, pp. 3329-3342, 2010.
- [5] L. Schlapbach and A. Züttel, "Hydrogen-storage materials for mobile applications," *Nature*, vol. 414, no. 6861, pp. 353-358, 2001.
- [6] K. L. Lim, H. Kazemian, Z. Yaakob, and W. W. Daud, "Solid-state Materials and Methods for Hydrogen Storage: A Critical Review," *Chemical engineering & technology*, vol. 33, no. 2, pp. 213-226, 2010.
- [7] [http://greenecon.net/solar-and-hydrogen-energy-economics/energy\\_economics.html](http://greenecon.net/solar-and-hydrogen-energy-economics/energy_economics.html).
- [8] T. Hua *et al.*, "Technical assessment of compressed hydrogen storage tank systems for automotive applications," *International Journal of Hydrogen Energy*, vol. 36, no. 4, pp. 3037-3049, 2011.
- [9] L. Zhou, "Progress and problems in hydrogen storage methods," *Renewable and Sustainable Energy Reviews*, vol. 9, no. 4, pp. 395-408, 2005.
- [10] M. Schlichtenmayer and M. Hirscher, "Nanosponges for hydrogen storage," *Journal of Materials Chemistry*, vol. 22, no. 20, pp. 10134-10143, 2012.
- [11] A. Züttel, P. Sudan, P. Maun, T. Kiyobayashi, C. Emmenegger, and L. Schlapbach, "Hydrogen storage in carbon nanostructures," *International Journal of Hydrogen Energy*, vol. 27, no. 2, pp. 203-212, 2002.
- [12] <http://slideplayer.com/slide/4218264/>.
- [13] T. Graham, "On the absorption and dialytic separation of gases by colloid septa," *Philosophical transactions of the Royal Society of London*, vol. 156, pp. 399-439, 1866.
- [14] M. Dornheim, "Thermodynamics of metal hydrides: tailoring reaction enthalpies of hydrogen storage materials," in *Thermodynamics-Interaction Studies-Solids, Liquids and Gases*: InTech, 2011.
- [15] A. Miedema, "The electronegativity parameter for transition metals: heat of formation and charge transfer in alloys," *Journal of the less common metals*, vol. 32, no. 1, pp. 117-136, 1973.
- [16] L. Schlapbach and A. Züttel, "Hydrogen-storage materials for mobile applications," in *Materials for Sustainable Energy*: Co-Published with Macmillan Publishers Ltd, UK, 2012, pp. 265-270.
- [17] J. Lennard-Jones, "JE Lennard-Jones, Trans. Faraday Soc. 28, 333 (1932)," *Trans. Faraday Soc.*, vol. 28, p. 333, 1932.

- [18] J. Huot, "Kinetics and Thermodynamics," in *Hydrogen Technology: Mobile and Portable Applications*, A. Léon, Ed. Berlin, Heidelberg: Springer Berlin Heidelberg, 2008, pp. 471-500.
- [19] T. B. Flanagan and J. D. Clewley, "Hysteresis in metal hydrides," *Journal of the Less Common Metals*, vol. 83, no. 1, pp. 127-141, 1982/01/01/ 1982.
- [20] E. Akiba and H. Iba, "Hydrogen absorption by Laves phase related BCC solid solution," *Intermetallics*, vol. 6, no. 6, pp. 461-470, 1998/01/01 1998.
- [21] T. Kabutomori, H. Takeda, Y. Wakisaka, and K. Ohnishi, "Hydrogen absorption properties of TiCrA ( $A \equiv V, Mo$  or other transition metal) BCC solid solution alloys," *Journal of alloys and compounds*, vol. 231, no. 1-2, pp. 528-532, 1995.
- [22] M. Okada, T. Kuriwa, T. Tamura, H. Takamura, and A. Kamegawa, "Ti-V-Cr b.c.c. alloys with high protium content," *Journal of Alloys and Compounds*, vol. 330-332, pp. 511-516, 1/17/ 2002.
- [23] B. Sakintuna, F. Lamari-Darkrim, and M. Hirscher, "Metal hydride materials for solid hydrogen storage: A review," *International Journal of Hydrogen Energy*, vol. 32, no. 9, pp. 1121-1140, 6// 2007.
- [24] M. D. Danford, "Hydrogen trapping and the interaction of hydrogen with metals," 1987.
- [25] J. C. Lippold, *Welding metallurgy and weldability*. John Wiley & Sons, 2014.
- [26] D. Fruchart *et al.*, "Nanocrystalline composite for storage of hydrogen," ed: Google Patents, 2011.
- [27] M. Rong, F. Wang, J. Wang, Z. Wang, and H. Zhou, "Effect of heat treatment on hydrogen storage properties and thermal stability of V68Ti20Cr12 alloy," *Progress in Natural Science: Materials International*, vol. 27, no. 5, pp. 543-549, 2017/10/01/ 2017.
- [28] K. Edalati, H. Shao, H. Emami, H. Iwaoka, E. Akiba, and Z. Horita, "Activation of titanium-vanadium alloy for hydrogen storage by introduction of nanograins and edge dislocations using high-pressure torsion," *international journal of hydrogen energy*, vol. 41, no. 21, pp. 8917-8924, 2016.
- [29] J. Huot, "High-pressure torsion," in *Enhancing Hydrogen Storage Properties of Metal Hybrides*: Springer, 2016, pp. 11-17.
- [30] T. Bibienne, J.-L. Bobet, and J. Huot, "Crystal structure and hydrogen storage properties of body centered cubic 52Ti-12V-36Cr alloy doped with Zr7Ni10," *Journal of Alloys and Compounds*, vol. 607, pp. 251-257, 9/15/ 2014.
- [31] A. Martínez and D. S. d. Santos, "Hydrogen absorption/desorption properties in the TiCrV based alloys," *Materials Research*, vol. 15, pp. 809-812, 2012.
- [32] S. Miraglia, P. de Rango, S. Rivoirard, D. Fruchart, J. Charbonnier, and N. Skryabina, "Hydrogen sorption properties of compounds based on BCC Ti1 - xV1 - yCr1 + x + y alloys," *Journal of Alloys and Compounds*, vol. 536, pp. 1-6, 9/25/ 2012.
- [33] N. Skryabina, D. Fruchart, N. A. Medvedeva, P. de Rango, and A. A. Mironova, "Correlation between the Hydrogen Absorption Properties and the Vanadium Concentration of Ti-V-Cr Based Alloys," in *Solid State Phenomena*, 2017, vol. 257, pp. 165-172: Trans Tech Publ.
- [34] S. Banerjee, A. Kumar, P. Ruz, and P. Sengupta, "Influence of Laves phase on microstructure and hydrogen storage properties of Ti-Cr-V based alloy,"

- International Journal of Hydrogen Energy*, vol. 41, no. 40, pp. 18130-18140, 10/26/ 2016.
- [35] K. Shashikala, S. Banerjee, A. Kumar, M. Pai, and C. Pillai, "Improvement of hydrogen storage properties of TiCrV alloy by Zr substitution for Ti," *international journal of hydrogen energy*, vol. 34, no. 16, pp. 6684-6689, 2009.
  - [36] T. Bibienne, V. Razafindramanana, J.-L. Bobet, and J. Huot, "Synthesis, characterization and hydrogen sorption properties of a Body Centered Cubic 42Ti–21V–37Cr alloy doped with Zr7Ni10," *Journal of Alloys and Compounds*, vol. 620, pp. 101-108, 2015/01/25/ 2015.
  - [37] P. Jain, C. Gosselin, N. Skryabina, D. Fruchart, and J. Huot, "Hydrogenation properties of TiFe with Zr 7 Ni 10 alloy as additive," *Journal of Alloys and Compounds*, vol. 636, pp. 375-380, 2015.
  - [38] P. Jain, C. Gosselin, and J. Huot, "Effect of Zr, Ni and Zr 7 Ni 10 alloy on hydrogen storage characteristics of TiFe alloy," *International Journal of Hydrogen Energy*, vol. 40, no. 47, pp. 16921-16927, 2015.
  - [39] Y. Leng, *Materials Characterization: Introduction to Microscopic and Spectroscopic Methods*. Wiley, 2009.
  - [40] [http://www.wikiwand.com/en/Scanning\\_electron\\_microscope](http://www.wikiwand.com/en/Scanning_electron_microscope).
  - [41] <http://www.ncl.ac.uk/nexus/techniques/edx.htm>.
  - [42] J. I. Goldstein *et al.*, "Electron Beam–Specimen Interactions," in *Scanning Electron Microscopy and X-ray Microanalysis: Third Edition* Boston, MA: Springer US, 2003, pp. 61-98.
  - [43] <http://publish.illinois.edu/x-raycrystallography/files/2014/12/Braggs-Law.jpg>.
  - [44] R. Jenkins, "X-Ray Techniques: Overview," *Encyclopedia of analytical chemistry*, 2000.
  - [45] R. Checchetto, G. Trettel, and A. Miotello, "Sievert-type apparatus for the study of hydrogen storage in solids," *Measurement Science and Technology*, vol. 15, no. 1, p. 127, 2004.
  - [46] P. American Institute of, B. H. Billings, and D. E. Gray, *American Institute of Physics handbook*. New York: McGraw-Hill, 1972.
  - [47] D. Bellon, A. Martinez, D. Barreneche, and D. dos Santos, "A structural study of the hydrogen absorption properties by replacing vanadium with zirconium in metal alloys," in *Journal of Physics: Conference Series*, 2016, vol. 687, no. 1, p. 012057: IOP Publishing.
  - [48] L. Zaluski, A. Zaluska, and J. O. Ström-Olsen, "Nanocrystalline metal hydrides," *Journal of Alloys and Compounds*, vol. 253-254, pp. 70-79, 1997/05/20/ 1997.
  - [49] J. Huot and M. Tournant, "Hydrogen sorption enhancement in cold-rolled and ball-milled CaNi<sub>5</sub>," *Journal of Materials Science*, journal article vol. 52, no. 20, pp. 11911-11918, October 2017.
  - [50] M. Tournant and J. Huot, "Hydrogen sorption enhancement in cold rolled LaNi<sub>5</sub>," *Journal of Alloys and Compounds*, vol. 595, pp. 22-27, 2014.